

UNIVERSITY OF OKLAHOMA

GRADUATE COLLEGE

DEVELOPMENT OF AN EMPIRICAL PROPELLER THRUST
MODEL USING EXPERIMENTAL MEASUREMENTS AND
COMPUTATIONAL FLUID DYNAMICS

A THESIS

SUBMITTED TO THE GRADUATE FACULTY

in partial fulfillment of the requirements for the

Degree of

MASTER OF SCIENCE

AEROSPACE ENGINEERING

By

ALEXANDER BRYANT

Norman, Oklahoma

2020

DEVELOPMENT OF AN EMPIRICAL PROPELLER THRUST MODEL USING
EXPERIMENTAL MEASUREMENTS AND COMPUTATIONAL FLUID DYNAMICS

A THESIS APPROVED FOR THE
SCHOOL OF AEROSPACE AND MECHANICAL ENGINEERING

BY THE COMMITTEE CONSISTING OF

Dr. Dibbon K. Walters, Chair

Dr. Thomas Hays

Dr. Ramkumar Parthasarathy

©Copyright by Alexander H. Bryant 2020
All Rights Reserved.

To my wonderful parents, Randy and Connie, and my older brother, Dillon:
Thank you guys for supporting me in all that I've ever done, whether it be in
athletics or academics. Your love, support, and sacrifices are the reasons I
am where I am today.

-Al

Acknowledgments

I would like to thank my advisor, Dr. Keith Walters, for allowing me to join the Applied Computational Fluid Dynamics research team, and for his guidance and support in my knowledge of the subject and my professional development. I would also like to thank Dr. Kumar Parthasarathy for pushing me to be the best student and best engineer I could possibly be, and Dr. Thomas Hays, for truly introducing me to the world of aeronautical engineering and igniting my passion for learning about all things aeronautics. To my fellow classmate and friend Jake Pannell, thank you for helping me get started when I joined the research team and for being a loyal friend through five years of school. Special thanks to Arrival 3D, Inc., for providing us with excellent geometry that was used in our simulations, to the Office of Naval Research for the funding of my research work, and also to fellow student Chris Hughes, who helped with setting up the experimental portion of this project. The support of the aforementioned people and groups cannot be overstated.

Abstract

Autonomous unmanned aerial vehicles (UAVs) are playing an ever-increasing role in naval operations. In order for these UAVs to safely operate autonomously in a wide range of conditions, robust control systems must be combined with a high-fidelity model of the thrust from the vehicle's propellers. The vast majority of experimental and computational fluid dynamics (CFD) studies on propeller thrust documented in the open literature have studied propeller thrust only as a function of RPM and axial advance ratio. For a UAV operating in the vicinity of the moving deck of a ship, operating conditions will also include crosswinds across the propeller disks and effects from the vehicle proximity to the ship deck. Currently, no experimental or computational studies provide an all-encompassing study into the entirety of a propeller's operating envelope. In this thesis, CFD is utilized to investigate the thrust performance of a small-scale propeller as a function of RPM, axial advance ratio, transverse advance ratio, and ground proximity. Experimental thrust measurements were also performed in order to validate thrust trends and provide an anchor for the thrust data from CFD. The thrust data from the CFD showed exceptional qualitative agreement with available experimental data while generally overpredicting thrust by 20 percent. The combination of the experimental and CFD data allowed for an accurate empirical thrust model to be developed that will permit UAVs to safely and effectively operate in a wide range of operating conditions. The results presented in this thesis highlight the critical role that both experimental and computational tools can play in propeller design and analysis.

Table of Contents

Acknowledgments.....	v
Abstract.....	vi
Table of Figures	x
List of Tables	xiv
Nomenclature.....	xv
Chapter I.....	1
Introduction.....	1
Chapter II	4
Literature Review.....	4
2.1 Experimental Studies	5
2.2 Computational Studies	9
2.3 Unresolved Issues	14
Chapter III.....	16
Propeller Performance Theory.....	16
3.1 Conventions	16
3.2 Theory.....	18
Chapter IV.....	20
Experimental Measurements.....	20
4.1 Experimental Setup.....	20
4.2 Experimental Procedures	24
4.2.1 Calibration.....	24
4.2.2 Thrust Measurements.....	25

4.3 Results.....	27
Chapter V	32
Computational Models.....	32
5.1 Reynolds Averaged Navier-Stokes Modeling	32
Chapter VI.....	35
CFD Case Setups	35
6.1 Propeller Geometry.....	35
6.2 Mesh Generation.....	36
6.3 Boundary Conditions	37
6.3.1 Static Cases	38
6.3.2 Advancing and Crosswind Cases.....	38
6.3.3 Ground Effect Cases	39
6.4 Numerical Methods.....	40
6.5 Computational Requirements	43
Chapter VII	44
CFD Results	44
7.1 Test Cases	44
7.1.1 Boundary Condition Tests	45
7.1.2 Transient vs Steady State.....	45
7.1.3 Turbulent vs Laminar.....	48
7.2 Static Cases	49
7.3 Advancing Cases.....	55
7.3.1 Ascending Flight.....	56

7.3.2 Descending Flight	58
7.4 Ground Effect Cases	61
7.5 Crosswind Cases	65
7.6 Final Empirical Thrust Model.....	71
7.6.1 RPM Dependence	72
7.6.2 Advance Ratio Dependence.....	73
7.6.3 Ground Effect Dependence.....	74
7.6.4 Crosswind Dependence.....	75
7.6.5 Complete Model	75
Chapter VIII.....	79
Conclusions and Future Work	79
8.1 Conclusions.....	79
8.2 Future Work.....	81
References.....	83

Table of Figures

Figure 1: Propeller dimensions and aerodynamic quantities	17
Figure 2: Cross-section of a propeller blade section.....	18
Figure 3: DD7x4.5 propeller.....	20
Figure 4: Airfoil sections at: a.) 0.25R b.) 0.5R c.) 0.75R d.) Blade Tip. NOTE: Not to scale....	21
Figure 5: Turnigy® Thrust Measurement Stand.....	22
Figure 6: Load cell for the thrust stand b.) Nodules that transmit force to load cell	22
Figure 7: Neiko 20713A Digital Tachometer	23
Figure 8: Motor, ESC, and battery used in the experiments	23
Figure 9: Applied known weights vs the averaged load cell output	25
Figure 10: Experimental setup for static, far field thrust measurements	26
Figure 11: Experimental setup for the ground effect thrust measurements.	27
Figure 12: Measured static thrust as a function of RPM	28
Figure 13: Static, far-field thrust coefficient as a function of RPM	28
Figure 14: Coefficient of thrust vs RPM at several wall proximities	29
Figure 15: C_T/C_{TOGE} for the DD7x4.5 and APC 11x5.5 for a range of h/D values	30
Figure 16: DD7x4.5 digital geometry used in the CFD studies.....	35
Figure 17: Computational domain boundaries with propeller shown within the domain.....	36
Figure 18: (a-b) Structured and unstructured meshes near propeller blade at span 0.7R	37
Figure 19: Groups of cells used as wall boundaries in ground effect simulations	40
Figure 20: Thrust convergence at 10,000RPM, a.) Static b.) $J = 0.375$ c.) $J = 0.50$ d.) $h = 4in$...	41
Figure 21: Thrust convergence at 10,000 RPM over a range of advance ratios	42
Figure 22: Thrust over a period of five blade rotations at 2000 RPM, $\mu = 0.25$	43

Figure 23: RVM Contours at span 0.7R at 10,000 RPM, a.) Instantaneous b.) Time-Averaged .	46
Figure 24: C_P vs s/c at span 0.7R, 10,000 RPM a.) Instantaneous b.) Time-Averaged.....	47
Figure 25: Ratio of C_T to C_{T0} vs J at 10,000 RPM using several turbulence models	48
Figure 26: Static thrust coefficient vs RPM from CFD and experimental measurement	50
Figure 27: RVM contours at span 0.7R a.) 1,000RPM b.) 5,000RPM c.) 10,000RPM d.) 15,000RPM.....	51
Figure 28: C_P vs s/c at span 0.7R, a.) 1,000 RPM b.) 5,000 RPM.....	52
Figure 29: C_P vs s/c at span 0.7R, a.) 10,000 RPM b.) 15,000 RPM.....	52
Figure 30: Contours of wall shear stress on the blade suction side a.) 1,000RPM b.) 5,000RPM c.) 10,000RPM d.) 15,000RPM	53
Figure 31: Friction coefficient vs s/c at span 0.7R at multiple RPM's.....	54
Figure 32: Static thrust vs RPM as predicted by CFD and experiments	55
Figure 33: C_T vs J over a range of RPMs.	56
Figure 34: RVM contours at 10,000 RPM at span 0.7R a.) Static b.) $J = 0.25$ c.) $J = 0.50$ d.) $J =$ 0.75.....	57
Figure 35: C_P vs s/c at span 0.7R, a.) Static b.) $J = 0.25$	58
Figure 36: C_P vs s/c at span 0.7R, a.) $J = 0.50$ b.) $J = 0.75$	58
Figure 37: RVM Contours at 10,000 RPM, span 0.7R a.) Static b.) $J = -0.125$	59
Figure 38: C_P vs s/c at 10,000 RPM, span 0.7R a.) Static b.) $J = -0.125$	59
Figure 39: Isosurface of $Q_{norm} = 0.75$ at 10,000 RPM, static.....	60
Figure 40: Isosurface of $Q_{norm} = 0.75$ at 10,000 RPM, $J = -0.125$	61
Figure 41: C_T vs RPM at a variety of h/D values	62
Figure 42: C_T/C_{TOGE} vs h/D for the DD7x4.5 (CFD and Experimental) and 11x4.5	63

Figure 43: C_P vs s/c at span $0.7R$, $10,000$ RPM a.) $h/D = 0.57$ b.) $h/D = 0.71$	63
Figure 44: C_P vs s/c at span $0.7R$, $10,000$ RPM a.) $h/D = 0.86$ b.) $h/D = 1.00$	64
Figure 45: C_P vs s/c at span $0.7R$, $10,000$ RPM a.) $h/D = 1.14$ b.) $h/D = 1.43$	64
Figure 46: Suction Side C_P vs s/c at span $0.7R$, $10,000$ RPM, at a variety of h/D values	65
Figure 47: C_T vs μ at several RPMs.....	66
Figure 48: Blade rotation angle Φ shown in relation to crosswind velocity field V_z	66
Figure 49: Contours of static pressure on the propeller blades' surface at $10,000$ RPM, $\mu = 0.25$, $\Phi = 0^\circ$ a.) suction side b.) pressure side.....	67
Figure 50: Contours of static pressure on the propeller blades' surface at $10,000$ RPM, $\mu = 0.25$, $\Phi = 45^\circ$ a.) suction side b.) pressure side.....	67
Figure 51: Contours of static pressure on the propeller blades' surface at $10,000$ RPM, $\mu = 0.25$, $\Phi = 90^\circ$ a.) suction side b.) pressure side.....	68
Figure 52: Propeller thrust as the blades rotate at $10,000$ RPM, $\mu = 0.25$	68
Figure 53: Contours of static pressure on the propeller blades' surface at $10,000$ RPM, $\mu = 0.00$, $\Phi = 0^\circ$ a.) suction side b.) pressure side.....	70
Figure 54: Contours of static pressure on the propeller blades' surface at $10,000$ RPM, $\mu = 0.25$, $\Phi = 0^\circ$ a.) suction side b.) pressure side.....	70
Figure 55: Contours of static pressure on the propeller blades' surface at $10,000$ RPM, $\mu = 0.75$, $\Phi = 0^\circ$ a.) suction side b.) pressure side.....	71
Figure 56: Contours of static pressure on the propeller blades' surface at $10,000$ RPM, $\mu = 1.25$, $\Phi = 0^\circ$ a.) suction side b.) pressure side.....	71
Figure 57: Anchored C_{T0} values vs RPM, with trendline shown.....	73
Figure 58: C_T/C_{T0} vs advance ratio values with trendline shown.	74

Figure 59: C_T vs C_{TOGE} vs h/D with trendline shown. 74

Figure 60: C_T/C_{T0} vs transverse advance ratio values with trendline shown..... 75

List of Tables

Table 1: Blade section specifications at different span-wise locations for the DD7x4.5 propeller	21
Table 2: List of equipment used for experimental measurements	24
Table 3: Recorded values of RPM and thrust, calculated C_T for static thrust tests	27
Table 4: Mean, standard deviation, and uncertainties at 7,999 RPM	31
Table 5: Impact of boundary conditions on thrust production at 10,000 RPM	45
Table 6: Static thrust at 10,000 RPM for steady-state and transient simulations	46
Table 7: Conversion between RPM and Re at 75 percent span	50
Table 8: Thrust predictions from empirical model vs that of CFD simulations	76
Table 9: Percent difference in thrust predictions from new model and old model.....	77

Nomenclature

c : Propeller Blade Chord

C_f : Skin Friction Coefficient

C_P : Coefficient of Pressure

C_T : Coefficient of Thrust

D : Propeller Diameter

h : Ground Proximity

J : Axial Advance Ratio

n : Rotational Speed, Revolutions per Second

OGE: Out of Ground Effect

Q : Torque

Q_{crit} : Q-Criterion

Q_{norm} : Normalized Q-Criterion

R : Propeller Radius

r : Span-Wise Location

Re : Reynolds Number

RPM: Rotational Speed, Revolutions per Minute

T : Thrust

u : Relative x-velocity

V_∞ : Relative Wind

V_z : Crosswind Velocity

V_y : Vertical Velocity

α : Aerodynamic Angle of Attack

θ : Blade Incidence Angle

ν : Kinematic Viscosity

Ω : Rotational Speed, Radians per Second

$\dot{\epsilon}$: Strain Rate

μ : Transverse Advance Ratio

ρ : Air Density

Φ : Blade Rotation Angle

ω : Vorticity

Chapter I

Introduction

In the past decade, the deployment and usage of small scale unmanned aerial vehicles (UAVs) have proliferated for a wide range of civilian and military applications. These applications range from racing and photography for civilians to land or ship-based reconnaissance operations for military purposes. On the military side, recent research and development efforts have been facilitated by the Office of Naval Research (ONR) towards providing small autonomous UAVs equipped with four or more propellers (commonly known as ‘quadrotors’) with the capability to conduct takeoff and landing operations off of naval ship decks in a wide range of weather and operating conditions. In order for a UAV to safely operate autonomously, its onboard control system must be equipped with an accurate empirical model for the thrust of its propellers over the entirety of its operating envelope.

Presently, there are three principal methods for mapping the operational space for a propeller’s thrust: analytical methods, experimental measurements, and numerical simulations. Analytical methods, though quicker and simpler than experimental or numerical methods, tend to incur a high degree of error in their thrust predictions and are limited by their underlying assumptions in the variety of operating situations they can accurately predict. These are usually used in preliminary design studies of propellers rather than mapping their entire operational space. Experimental methods using wind tunnels and force measurement devices provide the highest fidelity means of measuring a propeller’s thrust. Though they are often expensive in terms of time, resources, and required infrastructure, and also suffer from measurement uncertainties and effects from the testing setup, experimental studies can often provide a baseline for the final method used in propeller performance testing—numerical simulations. Numerical simulations, or

computational fluid dynamics (CFD) simulations, use physics-based models of the equations of fluid motion to resolve the velocity and pressure in the fluid-flow field. Often there is an attempt to validate CFD predictions using known experimental measurements. However, attention must also be paid to the computational intensity of the CFD study, as this will affect the overall cost in terms of time, CPU, and memory usage, for obtaining accurate results. Because of the underlying three-dimensional effects of propeller motion, CFD studies on propeller performance are most often performed in three dimensions, meaning computational cost will quickly grow with propeller size and with the complexity of the operating conditions.

This thesis presents an investigation of thrust performance of a Direct Drive (DD) 7x4.5 propeller using a combination of Reynolds-Averaged Navier-Stokes (RANS) based CFD studies and experimental measurements, with the objective of obtaining an accurate empirical model formulation relating thrust to rotational speed under a given set of operating conditions. The CFD studies evaluated propeller thrust as a function of advance ratio, crosswind speed, and ground proximity over a range of propeller rotational speeds. These studies primarily captured the trends of thrust across the whole of the operational space, with the knowledge that a degree of bias error was present. The experimental studies evaluated propeller thrust for the static case and for a number of ground proximities, again over a range of rotational speeds. These experimental measurements serve as an anchor for the trends captured by the CFD simulations, allowing for an accurate empirical thrust model to be developed for use in a ship-borne UAV's control algorithm. This empirical model will replace an older thrust model, typically used in UAV control systems, that does not take into account effects from advance ratio, crosswinds, or ground proximity. The goal is to develop an empirical model that will provide significant improvement over the previous

model, and will allow for the UAV's responses to environmental and operating conditions to improve considerably.

Chapter II

Literature Review

The aerodynamics of the flow governing the performance of the DD7x4.5 propeller are driven by incompressible, unsteady, low Reynolds number flow with separation and low levels of turbulence in parts of the flow field. Several studies concerning propeller performance in these conditions are available in the open literature. Some of these studies concern the experimentally measured thrust performance of propellers over a range of operating conditions, while others make use of CFD studies to attempt to achieve similar results. These CFD studies are often validated by comparing the results of the computational studies with experimental results. An overview of the literature concerning experimental and computational studies of propeller thrust performance is presented below. Unless stated otherwise, thrust coefficient, torque coefficient, power coefficient, advance ratio, and propeller efficiency respectively shall be denoted as follows throughout the literature review:

$$C_T = \frac{T}{\rho n^2 D^4} \quad (1)$$

$$C_Q = \frac{Q}{\rho n^2 D^5} \quad (2)$$

$$C_{Power} = 2\pi C_{Tor} \quad (3)$$

$$J = \frac{V}{nD} \quad (4)$$

$$\eta = J \frac{C_T}{C_{Power}} \quad (5)$$

Thrust is denoted by T, torque by Q, air density by ρ , propeller diameter by D, rotational velocity (rev/s) by n, and propeller forward velocity by V. Normalized ground proximity refers to the ratio of the propeller's ground proximity to its diameter (h/D).

2.1 Experimental Studies

Rossow (1985) performed an experimental study on the impact of the proximity of ground and ceiling planes on the thrust produced by a 0.325 m diameter helicopter rotor. In addition, two theoretical models were proposed to analytically study the impact of the floor and ceiling planes and were compared to the experimental data. Large plywood sheets were used to represent the ground and ceiling planes, which were placed from 0.08 to 1.92 rotor diameters and from 0.08 to 6 rotor diameters away from the rotor disk for the ground and ceiling planes, respectively. The rotor's rotational speed was varied from 3,000 to 5,000 RPM, resulting in a maximum Reynolds number (Re) of 167,000 at the rotor blade tips, based on the mean chord of the blades (2.65cm) and the rotational velocity at the blade tips. The resulting thrust data showed that thrust increased nearly linearly with the logarithm of the normalized ground distance (ratio of plane proximity to rotor diameter) of the rotor disk from the ground or ceiling plane, with a maximum increase in thrust of 20 percent at a normalized distance of 0.08 rotor diameters from a ground plane. The data showed that increase in rotor thrust began to appear when the normalized ground distance was reduced to 0.5 rotor diameters. The author attributed these effects from ground proximity to unsteadiness in the wake and in the propeller's inflow, as time-dependent flow variations were observed in the wake as it passed the edges of the floor plane. The author also formulated two theoretical models to attempt to predict this change in thrust using vortex cylinders above and below the rotor. The author's first model modeled the propeller's thrust using between 10 and 80 concentric vortex cylinders above and below the rotor. In a flow field without ground or ceiling planes, the vortex cylinders are semi-infinite in length, which gives them the characteristic of inducing at a constant downwash inside and a zero downwash outside the cylinder at the rotor disk. If the rotor is near a ground or ceiling plane, the velocity field couples the inboard and outboard

propeller blade segments because both sets of vortex cylinders contribute to the downwash at the rotor disk. With this formulation, the calculated downwash velocity through the rotor decreases, increasing thrust. Though this first model accurately captured the qualitative effects from the ground and ceiling planes, thrust was overpredicted by 10 percent across a range of normalized ground distances, and 15 percent across a range of normalized ceiling distances. The second model aimed to improve on the first model by eliminating the cylinder immediately below the ground plane. Though this model violates the no-flow-through condition at a ground plane, the change produced excellent agreement with experimental data for thrust as a function of normalized ground and ceiling proximity, with thrust measurements within experimental uncertainties (3 percent).

Brandt (2005) performed a number of experimental studies detailing the performance of small-scale propellers at low Re (below 100,000 according to the chord at 75 percent span) in both dynamic and static conditions. The experiments were performed in the low speed wind tunnel at the University of Illinois-Urbana Champaign (UIUC). Thrust and torque measurements were made using a load cell outside of the tunnel. Measurements of static thrust and torque were made for propellers of varying diameter (7in to 14in) over a range of rotational speeds (between 2,500 and 7,000) for each propeller, and each was again measured with the wind tunnel turned on over a range of advance ratios at several rotational speeds. Brandt noted that, in the static case, propeller thrust coefficient often decreased by more than five percent per 1,000 RPM below Reynolds numbers of approximately 30,000, and that propeller thrust coefficient increased slowly (between 0.5 and three percent per 1,000 RPM) in a linear fashion over most of the rotational speed range regardless of propeller selection. Brandt also noted that propeller thrust usually decreased to zero at advance ratios between 0.5 and 1 due to decreasing aerodynamic angle of attack on the blades with increasing advance ratio.

Lee et al. (2010) studied the impact of ground proximity on the fluid dynamics of a hovering rotor using a combination of flow visualization and phase-resolved particle image velocimetry (PIV). The authors used a two bladed rotor of diameter 86mm that was spun at rotational speeds between 2,100 RPM and 3,600 RPM, which corresponded to a maximum Re of 42,170. In addition to measuring the thrust and power exerted by the rotor at four distances from the ground, the authors used both illuminating submicron tracer particles (flow visualization) and PIV to study the effects of ground proximity on the propeller vortical wake. The authors found that the rotor wake and its downwash are subjected to powerful curvature and straining effects as they are deflected into a radially outward direction at the ground plane. The tip vortices were found to induce flow velocities that were significantly unsteady if they reached the ground plane without undergoing substantial diffusion. The authors documented the effects of the ground on the rotor performance through a combination of flow visualization photographs using high speed cameras, sensors to measure thrust and torque, PIV to produce high fidelity plots of the velocity field of the rotor wake. The authors noted that the changes observed in the flow field led to the thrust coefficient at a constant power level increasing by 40 percent at a normalized ground distance of 0.125 rotor diameters when compared to the thrust coefficient out of ground effect (normalized ground distance of 1.5 rotor diameters). The constant-thrust power coefficient at 0.125 rotor diameters decreased by 35 percent when compared to the power coefficient at 1.5 rotor diameters.

Deters et al. (2014) experimentally evaluated the performance of 27 off-the-shelf propellers and four 3D-printed propellers in order to quantify the effect of operating in the low Reynolds number regime ($Re < 100,000$ as defined at the chord at 75 percent span). The propellers ranged in diameter from 2.25in to 9in. The tests were performed in the UIUC low speed wind tunnel. Static thrust and torque, as well as dynamic thrust and torque, were recorded for each propeller

over an RPM range from 5,000 to 27,000 using load cells outside of the tunnel. As previously noted by Brandt (2005), static thrust coefficient increased linearly with increasing RPM (and by extension, Reynolds number), usually by two to four percent per 1,000 RPM. In addition to the static thrust coefficient, static power coefficient often decreased linearly with RPM at a similarly slow rate (typically one percent per 1,000 RPM). In dynamic conditions when advance ratio was nonzero, propeller efficiency saw increases of up to 10 percent between the lowest tested and highest tested RPMs (and therefore, Reynolds number) when testing at the same advance ratio. The authors noted that the maximum calculated efficiency values for the propellers tested were between 60 and 65 percent, well short of the 85 percent efficiency achieved by some propellers at higher Reynolds numbers. The authors attributed this efficiency deficit to increased drag on the propellers at lower Reynolds numbers, leading to increased power consumption, and also to effects from turbulent boundary layers at higher Reynolds numbers.

Cai et al. (2019) experimentally studied the effect of extreme ground effect on the performance of several commercially available propellers meant for use in small UAVs. The authors aimed to use propellers that were large enough to avoid the effects of low Reynolds numbers, while also still usable with conventional electric hobby-type motors. The diameters of the propellers used were 11in, 14in and 17in. The propellers studied had the following combinations of diameter and pitch (in inches): 11x5.5, 11x7, 14x7, 17x7, 17x10, and 17x12. The authors studied propeller diameter and pitch in various combinations to examine trends in thrust improvement and/or power reduction with closer ground proximity. Data on thrust and torque was gathered using a six-component force/moment balance, with the change in ground proximity achieved by moving the experimental setup closer to a wall. The authors found significant effects on thrust and power resulting from ground increased proximity, with up to a 15 percent increase

in the thrust coefficient achieved at a constant power level at a normalized ground distance of 0.25 propeller diameters when compared to thrust coefficient out of ground effect (normalized ground distance of 1.5 propeller diameters). Power coefficient at a constant thrust level was reduced by up to 18 percent at a normalized ground distance of 0.25 propeller diameters when compared to power coefficient out of ground effect (normalized ground distance of 1.5 propeller diameters). The authors also found that the lower the ratio of pitch to diameter, the larger the impacts from ground proximity on thrust and power production, with symmetric results whether the ground-plane was behind or ahead of the propeller. The authors postulated that these effects could stem from the aerodynamic angle of attack on the blades being influenced by the ground plane, but conceded that flow visualization was needed to ascertain the physical phenomenon responsible for the changes to thrust and power. The authors proposed an expression combining the effects of ground proximity, diameter, and pitch that would result in one curve of power reduction when compared to the normalized ground distance.

2.2 Computational Studies

Rumsey et al. (2002) reviewed the current capabilities of CFD methods in predicting the aerodynamic characteristics of two-dimensional airfoils and three-dimensional finite wings in a variety of configurations using a variety of CFD tools. In general, if best practices for grid spacing, turbulence modeling, and laminar-turbulent transition are followed, the author found that lift and drag could be predicted with reasonable accuracy at angles of attack below stall. These conclusions were based on research primarily conducted for $Re < 1 \times 10^7$ and at subsonic Mach numbers, so their validity cannot be presumed at other conditions. Reynolds number effects can be predicted accurately in two-dimensional cases; however, predictions of Reynolds number effects in three-

dimensional configurations were inconsistent. With regard to stall, two-dimensional CFD was shown to be unreliable in predicting stall, with the maximum lift usually being over-predicted. In addition, three-dimensional CFD was also found to be unreliable in predicting stall; however, the author notes that there have been fewer of these applications to date. The authors also notes that compressible RANS codes performed the best at predicting the maximum lift and drag of two-dimensional airfoils. The authors conclude by summarizing the challenges faced by CFD users in the coming years: accurately modeling unsteady effects, the inadequacy of current turbulence models, and the lack of high fidelity geometries available for use in the simulations, with the last being the most dominant factor.

Turner (2010) used Ansys FLUENT to perform CFD simulations to design and optimize a small propeller for use on a micro-air vehicle (MAV). The MAV in question weighed 150g, with a wingspan of 0.15m, and operated at a forward flight speed of 11.0 m/s. The author first conducted CFD studies on a variety of two-dimensional airfoils in order to surmise the optimal airfoil(s) to be used for the MAV's propeller blades. The effects of airfoil thickness, camber, angle of attack, position of maximum camber, position of maximum thickness, and Reynolds number on lift-to-drag ratio were studied in order to find optimums. The simulations were performed in a rectangular domain of 10 chord lengths in height and 26 chord lengths in length, with the airfoil positioned five chord lengths from an inlet and five chord lengths from the top and bottom of the domain. A pressure outlet was placed 20 chord lengths behind the airfoil. Meshes for the studies were unstructured and hexahedral, and typically contained 60,000 to 85,000 cells. This corresponded to a minimum grid size of 4.8×10^{-6} m to 1.2×10^{-6} m. The author chose to use the realizable $k-\epsilon$ turbulence model with the enhanced wall treatment function applied. This model was used for both the two-dimensional and three-dimensional testing. Solution methods were second order, with

standard pressure treatment, and the simulations took typically 4,000 iterations and two hours for all equations to converge to residuals of 10^{-12} or lower. For simulating a full propeller in a three-dimensional space, the propeller geometry was meshed inside of a rotating reference frame within the larger domain. Typical cell sizing for a tetrahedral mesh was 3×10^{-5} m for a propeller of 0.1m diameter and 0.0125m chord length. The tetrahedral mesh was converted to a series of polyhedral grid elements. The diameter of the interior, rotating cell zone was set to 1.5 propeller diameters and length to 3.5 propeller diameters. The diameter of the outer, stationary zone was set to four propeller diameters and the length to seven propeller diameters. The incompressible, unsteady RANS equations were used with solution methods similar to the two-dimensional cases. All simulations were converged to residual values of 10^{-7} where possible, and where residuals reached steady state at higher values the result was assumed to be converged. This typically took between 600-800 iterations and 5-6 hours of computation time. The highest propeller efficiency achieved by a design which satisfied the thrust requirement of 0.24N was 60.7 percent. This substantiates the findings from Deters et al. (2014) that the maximum efficiency achievable in the low Re regime ($Re < 100,000$ as defined by the chord at 75 percent span) was between 60 and 65 percent. The final propeller design was an 8cm diameter propeller with a mean chord of 1.25cm that made use of a NACA 2309 airfoil section. The operating RPM for this design was 20,000 in cruise conditions. The author found that propeller and airfoil performance deteriorated significantly for $Re < 30,000$, and that the use of a cambered airfoils section yielded improvements in propeller efficiency of up to 10 percent when compared to symmetric airfoil sections due to higher lift-to-drag ratios. All CFD results were verified using an analytical model for propeller thrust predictions.

Zhang et al. (2015) used Ansys FLUENT to analyze changes in propeller performance in advancing flow and in crosswind conditions. The authors used a multiple reference frame approach (MRF) similar to Turner (2010). The propeller studied was of 10 in diameter with a maximum RPM of 7,000 corresponding to a maximum Reynolds number of around 100,000 at 75 percent span. The boundaries of the outer, stationary domain were set as velocity inlets, allowing for both crosswinds and advancing flow to be simulated. Sliding mesh technology was used that allows for the interface between the inner rotating zone and the outer stationary zone. The simulations were run using the incompressible, unsteady RANS equations with the Detached-Eddy-Simulation as the turbulence model. The residual error convergence precision was set to 10^{-3} . For the advancing cases, thrust was shown to decrease to zero between advance ratios of 0.6 and 0.8 for all RPMs tested. For the crosswind cases run, thrust was nearly constant with respect to crosswind speed at all RPMs up to a crosswind velocity of 8.0 m/s. The authors did not offer an explanation for the decrease in thrust produced with increasing advance ratio, nor did they perform any validation of the CFD by comparison to analytical calculations or experimental measurements.

Kutty and Rajendran (2017) used Ansys FLUENT to examine the performance of the APC Slow Flyer propeller and compared the results to available experimental data. The propeller was of 10in diameter and 7in of pitch. The digital propeller geometry was generated by joining blade sections every half inch along the span of the propeller instead of using 3D scanning. The authors employed the MRF approach akin to the method used by Turner (2010) and Zhang et al. (2015). The propeller was set in a cylindrical zone sized to 1.1 times the propeller's diameter, with the length of the zone being 0.4 times the propeller's diameter. The outer stationary zone was a cube with side lengths of eight propeller diameters. The mesh used was generated in the FLUENT workbench without modification and contained 4×10^6 cells. Boundary conditions were set as

follows: the inlet face of the stationary zone was set as a velocity inlet with turbulence intensity 0.1 percent, with the outlet face being set for outflow conditions. The simulations were run at a constant propeller RPM of 3,008, corresponding to a Reynolds number of 50,804 at 75 percent span. Inlet velocities between 2.44 m/s and 10.15 m/s were used to simulate advancing flow, and coefficients of thrust, coefficients of power, and efficiency were calculated for each case. The studies were run using the standard $k-\omega$ turbulence model. The percentage error in thrust coefficient when compared to experimental measurements remained below five percent until high advance ratios ($J > 0.7$). Both power coefficients and efficiencies were consistently over predicted by around five percent until advance ratio exceeded 0.7. The authors' explanation for these discrepancies were offered only as "three dimensional effects".

Kutty et al. (2017) conducted a review of experimental and numerical research on the performance of both conventional and unconventional propeller designs. The review covers propeller blades used for fixed-wing manned aircraft, UAVs, marine vehicles, and wind turbines. The author discussed the experimental studies performed by Brandt (2005) and Deters et al. (2014) (discussed above), and also examined several other wind tunnel tests of propeller performance at low Reynolds numbers. The data from one of these experimental studies was compared to results computed using XFOIL. Significant error of over 20 percent was present in thrust predictions, leading the authors to conclude that experimental measurement is preferred to panel codes such as XFOIL or XFLR5. The authors went on to comment on a number of computational studies performed for the same purposes. The most popular and successful method to study propeller performance using CFD is the formerly discussed multiple reference frame approach. These studies were performed on both marine and airborne propellers, with one only using $\frac{1}{4}$ of the propeller's geometry (one of four blades) and consequently, $\frac{1}{4}$ of the operating domain. The

simulations were used to predict thrust and torque for both static and advancing cases, and results compared well with experimental data in the majority of cases. RANS modeling using the standard $k-\epsilon$ turbulence model was the most popular turbulence model for most studies done in the low Reynolds number regime, although transitional models were also used in a few studies. The size of domains used in the studies varied widely, with some similar in size to those used by Turner (2010) and others making use of domains with lengths on the order of 30 propeller diameters and diameters on the order of 20 propeller diameters. There was no significant effect from these size differences on the accuracy of the simulations observed in any of these studies. The paper also discusses the performance of unconventional propeller designs, such as propellers with serrations on the leading edge of the airfoil sections, slotted blade designs, and variable diameter designs. The performance of these unconventional designs was generally tested using experimental measurement in low-speed wind tunnels. The author concludes by stating that although experimental analysis is still the most accurate and reputable form of testing, current CFD capabilities for studying propeller performance are accurate enough in most cases to be used for quicker turnaround time in propeller design. This is especially true when experimental data is available for validation.

2.3 Unresolved Issues

The papers above show that studies investigating propeller performance are often performed by using numerical simulations in conjunction with experimental measurements. For propellers operating at low Reynolds numbers, experimental performance data is plentiful for static operations, advancing operations, and to a lesser extent, operations in ground effect. Performance data in crosswind operations (flow across the propeller disk) is not readily available for small scale

propellers. The majority of available numerical studies utilized the multiple reference frame approach using either the $k-\varepsilon$ or SST $k-\omega$ turbulence models. These models present their own problems for simulating propellers at low Reynolds numbers, casting doubt on whether the thrust predictions from simulations that use these models at low Reynolds numbers are to be trusted. In addition to concerns about computational accuracy, the study performed by Kutty and Rajendran (2017) used a 3D propeller geometry that was not a precision replica of the actual propeller used in the experimental testing used to validate their simulations, casting doubt on whether the thrust predicted by CFD was artificially lowered by poor geometry. The discretization methods for these studies were typically second-order accurate with relatively fine grids. Computational demand was generally high, with most studies taking 5+ wall clock hours per case. Generally, these centered on static performance and advancing performance. Detailed numerical investigations into the performance of propellers in ground effect or in crosswinds are lacking.

Chapter III

Propeller Performance Theory

The analysis of propeller performance is primarily executed using a variety of non-dimensional quantities, allowing propeller performance to be quantified across a wide range of operating and environmental conditions. This section will detail the conventions and terminology that will be used for the remainder of this thesis.

3.1 Conventions

The conventions that will be used in this thesis to define propeller dimensions and aerodynamics are outlined below in Figures 1 and 2. The CFD simulations were performed in a Cartesian coordinate system, with the origin being located in the middle of the propeller hub. The y-axis acted as the axis of rotation, with the propeller rotating in the x-z plane. The span-wise location r can be calculated using x and z-coordinates. These conventions will hold whether the reference frame is being rotated around a stationary propeller or the propeller itself is being spun within a stationary reference frame. When the propeller is said to be operating in crosswind conditions, the relative wind V_∞ acts in the same direction as the spinning motion of the propeller on the retreating side, and adds to the flow velocity seen by the advancing blade. This relationship of the rotational speed and the relative wind to u , the total relative airspeed seen by the blades, can be seen in Figure 2. The relative blade airspeed will also depend on the span-wise location r . When the propeller is advancing in the y-direction (i.e. ascending or descending), a y-velocity component is introduced that impacts the aerodynamic angle of attack seen by the blades. This is also illustrated below in Figure 2. When the propeller is ascending in the y-direction, the effective angle of attack on the blades is decreased. When the propeller is descending, the effective angle of attack

is increased. The convention shall be that V_y is reported as positive during ascending flight, and negative during descending flight. The top side of the blade section, which will experience large negative pressures during operation, will be known as the suction side, while the bottom side will be known as the pressure side.

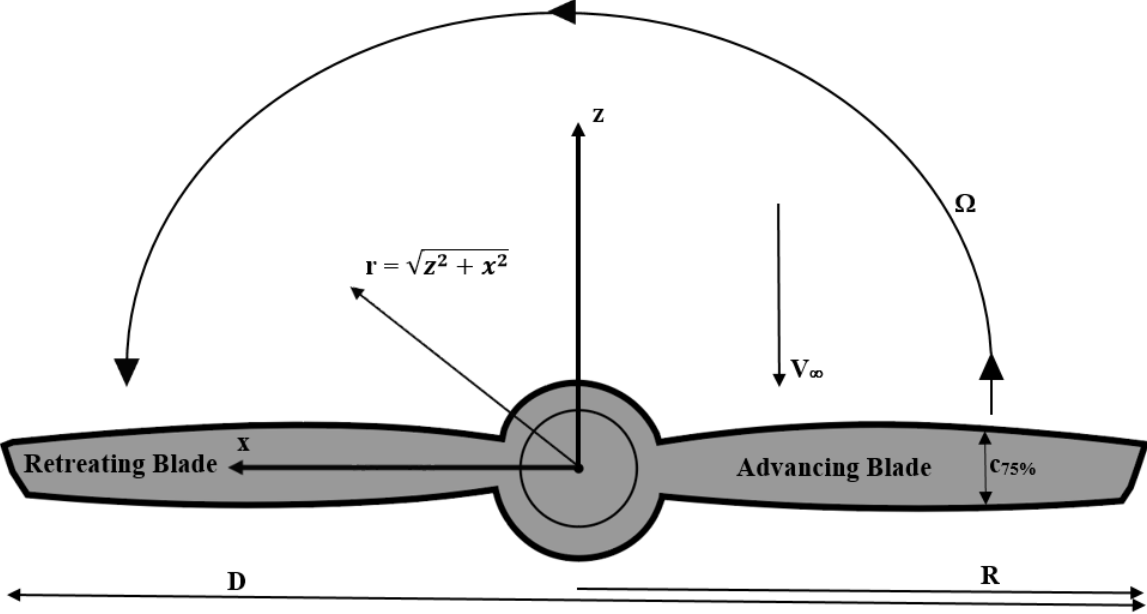


Figure 1: Propeller dimensions and aerodynamic quantities

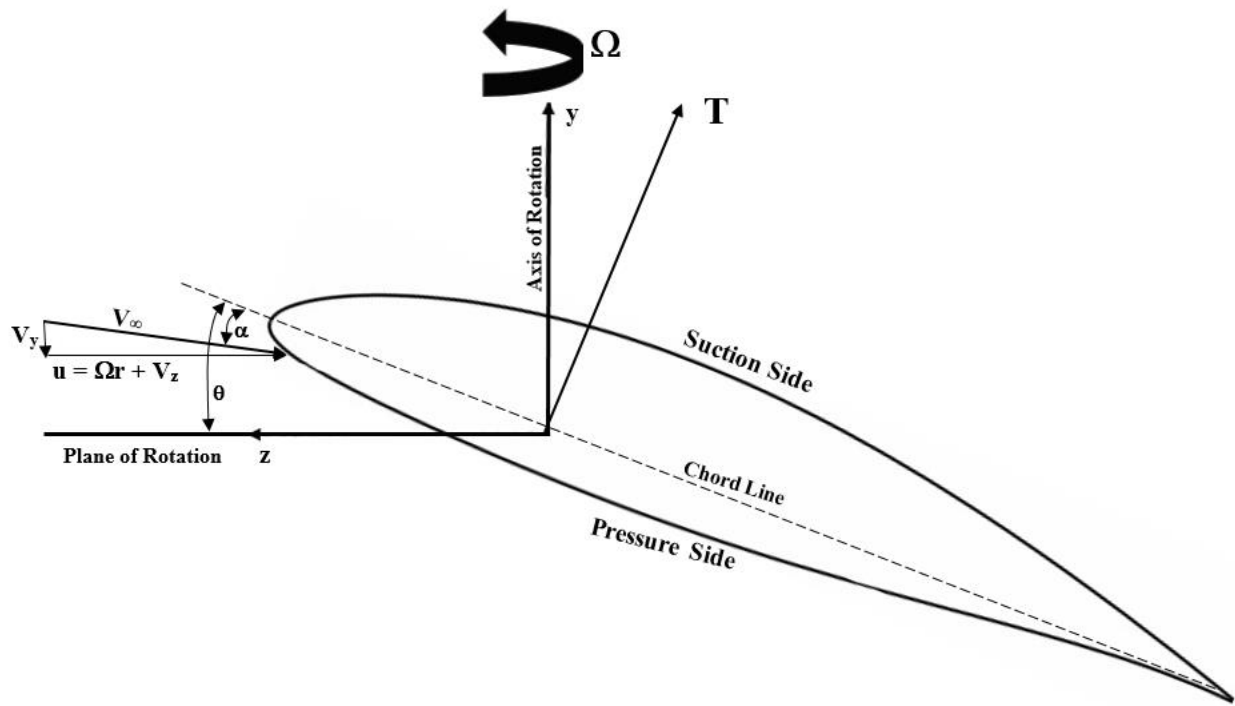


Figure 2: Cross-section of a propeller blade section

3.2 Theory

In order to accurately describe propeller performance, several non-dimensional quantities are used in order to ensure that the performance can be easily described and quantified for all atmospheric and operating conditions. The coefficient of thrust is a function of both propeller design and of the operating conditions of the propeller, and can be expressed as

$$C_T = \frac{T}{\rho n^2 D^4} = f(RPM, J, h/D, \mu) \quad (6)$$

Here T denotes thrust, n is rotational speed expressed in revolutions per second, h is distance from propeller plane to ground, D is propeller diameter, and ρ is the ambient air density. For static conditions, C_T is denoted as C_{T0} . The axial advance ratio can be described as how far the propeller moves axially in one complete revolution of its blades and is denoted as

$$J = \frac{V_y}{nD} \quad (7)$$

For crosswind conditions, the transverse advance ratio is defined as the ratio of the freestream velocity across the propeller disk to the speed of the blades at their tips. It is denoted as

$$\mu = \frac{V_z}{\Omega R} \quad (8)$$

This ratio is one when the relative airspeed experienced by the retreating blade is zero. The Reynolds number is defined with respect to the blade chord at 75 percent of the propeller's radius and the corresponding relative airspeed u :

$$Re = \frac{\Omega r_{75\%} c_{75\%}}{\nu} = \frac{u_{75\%} c_{75\%}}{\nu} \quad (9)$$

Chapter IV

Experimental Measurements

In order to provide anchor data for the trends that will be captured by the CFD simulations, the static performance of the DD7x4.5 propeller was experimentally evaluated across a range of RPMs. In addition to the static, far-field cases, propeller performance in ground effect was measured across the operating RPM range at several ground proximities in order to validate the data from the CFD simulations.

4.1 Experimental Setup

The propeller used in both the experimental and numerical studies was the DD7x4.5 propeller, illustrated below in Figure 3. The propeller is constructed using carbon fiber and has a diameter of seven inches (17.78cm) with 4.5 inches of pitch (11.43cm), with a pitch-diameter ratio of 0.643. It has a maximum operational RPM of 15,000. Blade incidence (θ) and chord length distributions as well as cross sections of the blades at several radial locations are shown below in Figure 4 and Table 1. The airfoil sections shown in Figure 4 are not to scale.

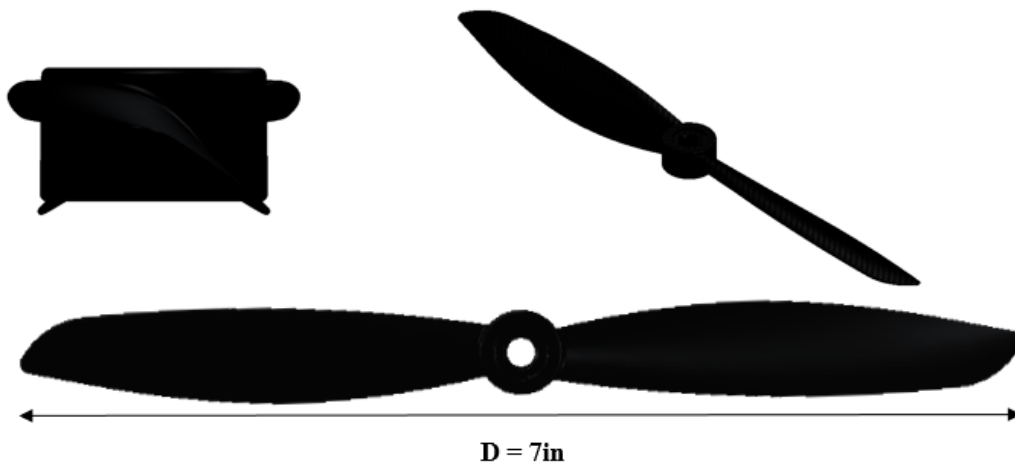


Figure 3: DD7x4.5 propeller

Table 1: Blade section specifications at different span-wise locations for the DD7x4.5 propeller

r/R	Chord (cm)	Blade Incidence ($^{\circ}$)	Maximum Camber (Percent of Chord)	Maximum Thickness (Percent of Chord)
0.25	1.594	29.62	9.89	19.18
0.50	1.863	32.22	7.53	16.43
0.75	1.531	28.11	6.22	15.91
0.95	0.543	19.40	4.22	12.68

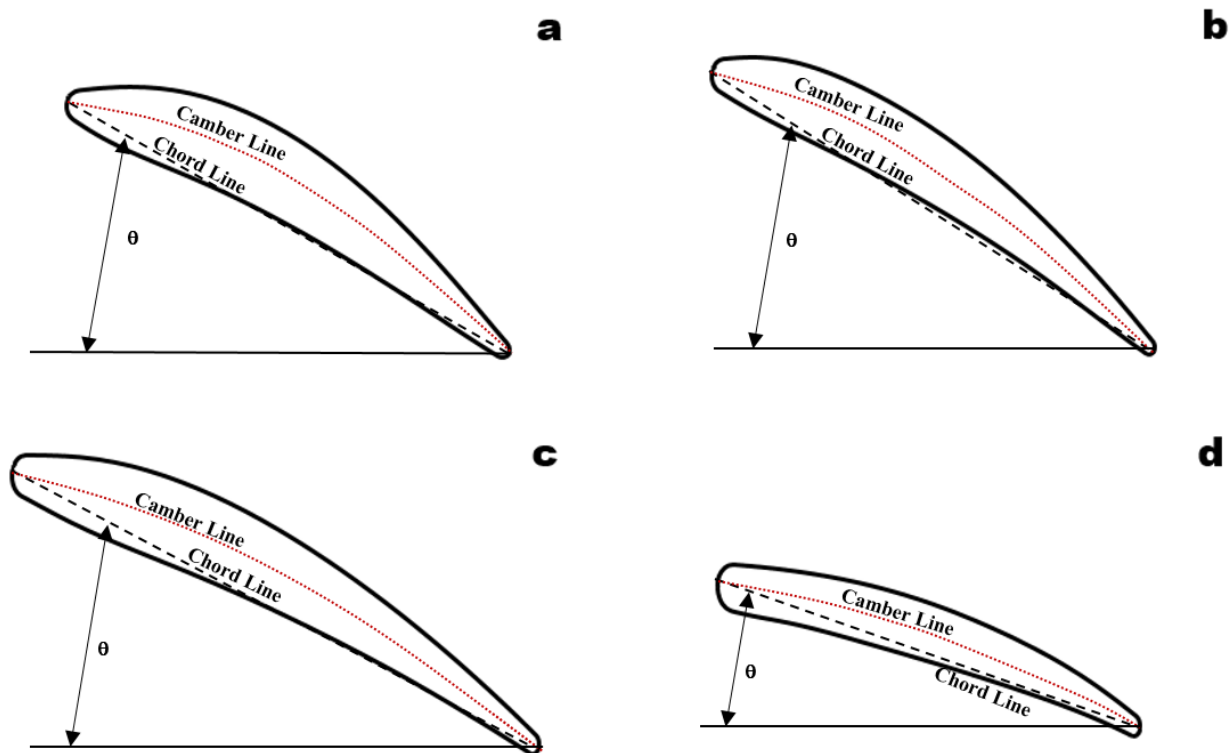


Figure 4: Airfoil sections at: a.) 0.25R b.) 0.5R c.) 0.75R d.) Blade Tip. NOTE: Not to scale

The commercially available Turnigy® Thrust Measurement Stand was used during the experiments. The thrust stand is constructed using stainless steel, and makes use of a load cell capable of measuring thrust values up to 49N. The propeller is attached to a bracket that is attached to a plate above the rest of the stand, and the plate is secured to the rest of the stand via two low-friction circular tracks that ensure forces are exerted only on the load cell. A small nodule on the

plate pushes on the load cell whenever a force is applied to the bracket, and the analog signal from the load cell is transmitted to a microprocessor that converts the analog signal to a calibrated thrust measurement. The load cell's output is given in grams. To ensure that propeller thrust in both directions could be measured, a second nodule was added to the mounting plate. The thrust stand and its various components are shown below in Figures 5 and 6.



Figure 5: Turnigy® Thrust Measurement Stand

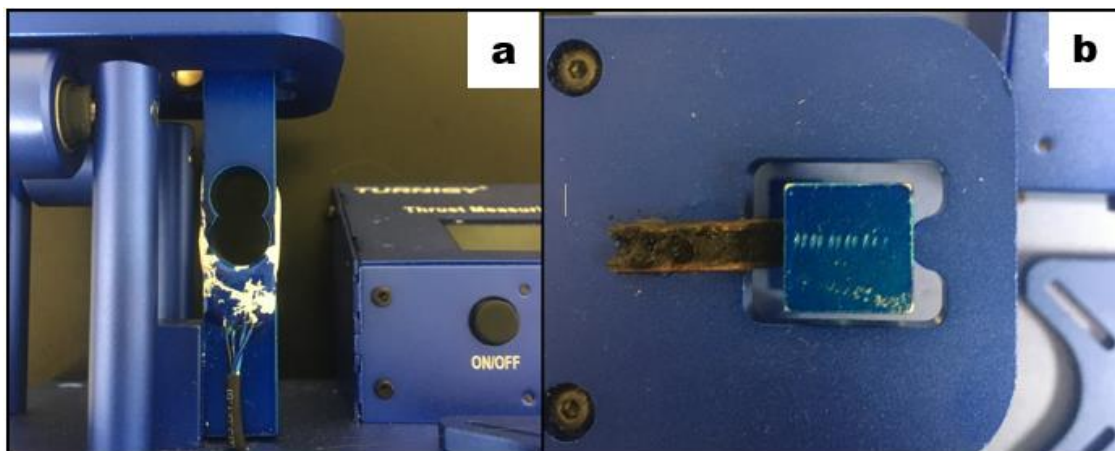


Figure 6: Load cell for the thrust stand b.) Nodules that transmit force to load cell

To measure RPM, the Neiko 20713A Digital Tachometer was utilized. The tachometer uses a laser pointed directly at reflective tape placed on the propeller to measure RPM. The RPM measurements are recorded at a sampling time of one second. The tachometer is shown below in Figure 7.



Figure 7: Neiko 20713A Digital Tachometer

To operate the propeller, an RC A2212 1400KV Brushless Motor and a 30A Electric Speed Controller (ESC) were paired with a two cell 7.4V Lithium-Polymer (LiPo) battery. The motor, ESC, and battery are pictured below in Figure 8.



Figure 8: Motor, ESC, and battery used in the experiments

The experiments were performed without the use of a digital data acquisition system. To record data for uncertainty analysis and processing, and also to ensure uncertainties were minimized, the readouts of RPM and thrust were recorded on video throughout the entirety of the experiments. This allowed data for RPM and thrust to be sampled at two second intervals over 10 second periods during the experiments. The videos were taken using an iPhone 6S video camera. For values of temperature and atmospheric pressure needed to calculate the density of air, the Norman, OK Mesonet data was used. The summary of the equipment used in the experiments and their accuracies and least counts are tabulated in Table 2.

Table 2: List of equipment used for experimental measurements

Instrument	Accuracy	Least Count
Neiko 20713A Digital Tachometer	$\pm 0.05\%$	1 RPM
Thrust Measurement Stand	± 10 grams	1 gram
RC A2212/10T Brushless Motor	-	-
RC 30A ESC	-	-
Turnigy® 2S 7.4V LiPo Battery	-	-
Direct Drive 7x4.5 Propeller	-	-
FrSky 8-Channel RC Reviver	-	-
FrSky RC Transmitter	-	-
iPhone 6S Video Camera	-	-

4.2 Experimental Procedures

4.2.1 Calibration

Before measurement of propeller thrust could be recorded, calibration of the thrust measurement stand was necessary. To perform this, a weight and pulley system was used to apply known weights to the load cell, and the corresponding load cell outputs were recorded. Twelve different weights were applied to the load cell, ranging from 0.89N to 11.1N. To account for effects from hysteresis, they were first applied in an unloading fashion, then were unloaded. Differences

between loading and unloading in load cell outputs due to hysteresis were generally less than five percent. At each value of known weight, this resulted in two recorded values for the load cell output. The average of the two was taken, and the results plotted as shown in Figure 9. The calibration resulted in the expected linear relationship between applied force and load cell output. This calibration was used to convert raw data from the experiments to true thrust data.

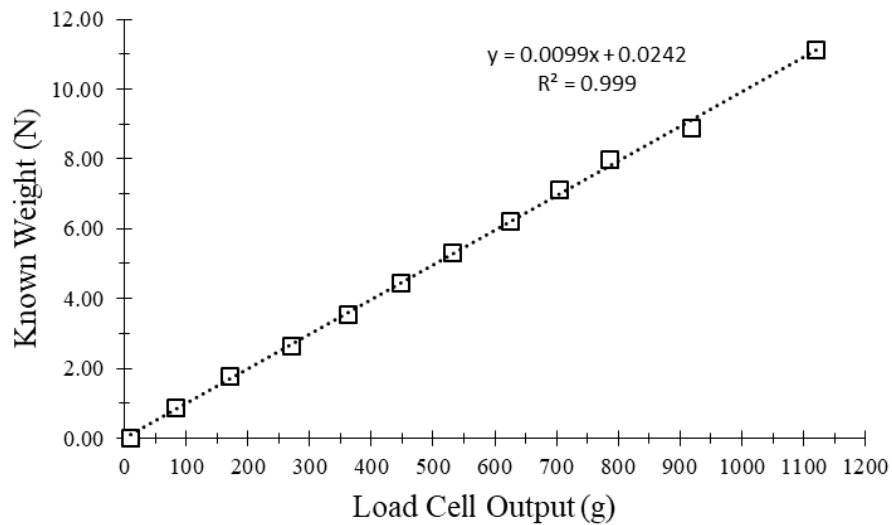


Figure 9: Applied known weights vs the averaged load cell output

4.2.2 Thrust Measurements

To obtain static thrust data for the DD7x4.5 propeller, the propeller was secured to the motor in a manner where the thrust vector was pointed towards the load cell, necessitating the addition of the wooden nodule seen in Figure 6b. This ensured that the structure of the thrust stand did not impact the propeller’s outflow. The reflective tape was placed at a span of 0.90R on the suction side of the propeller’s blade. This positioning allowed for convenient use of the tachometer by keeping the tachometer’s digital readout in the same video frame as the load cell output. The entire apparatus was clamped to the top side of a metal stool and placed outdoors well away from

any walls or obstructions to ensure that conditions were truly far-field. To ensure that conditions in the area were static, the experiments were performed on a day with minimal to no wind, and the apparatus was placed in an area sheltered from wind. The experimental setup can be seen below in Figure 10.



Figure 10: Experimental setup for static, far field thrust measurements

To run the experiment, the button activating the tachometer was held down for its entirety. The load cell output was then tared, the video camera was turned on, and the operator with the RC transmitter increased the throttle at approximately 1,000 RPM increments. At every increment, the propeller RPM was held constant for 15 seconds. For the first five seconds, the thrust and RPM outputs were allowed to arrive at steady state. For the next 10 seconds, load cell and RPM data were sampled every two seconds from the video. This was repeated until the motor reached its maximum obtainable RPM. For the ground effect measurements, this procedure was repeated with a wall 4in, 5in, 6in, 7in, and 8in from the propeller disk.

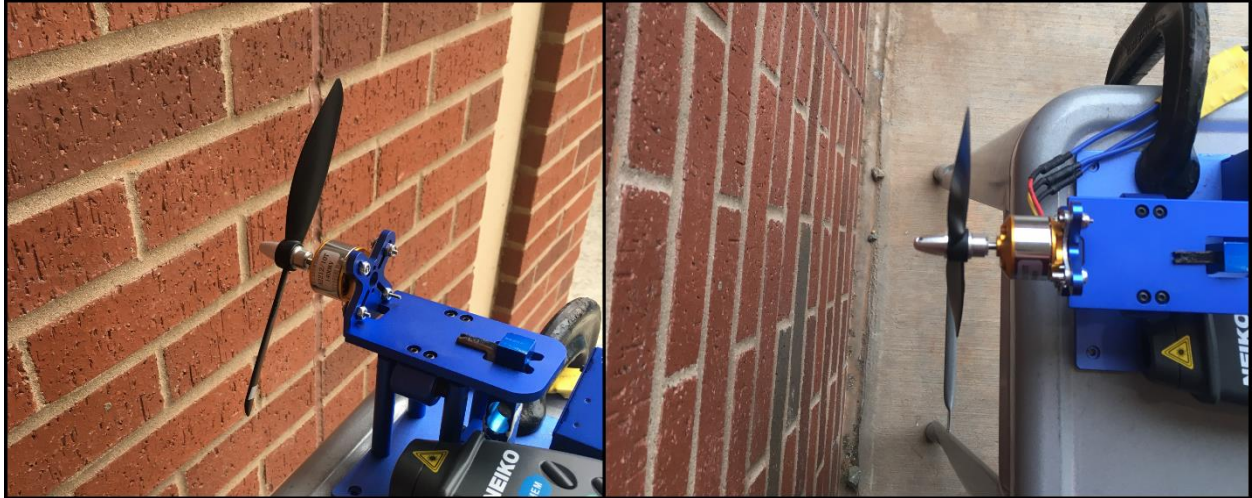


Figure 11: Experimental setup for the ground effect thrust measurements.

4.3 Results

The recorded values of RPM, thrust, and the calculated C_T for the static thrust tests are presented below in Table 3, and a thrust as a function of RPM is included in Figure 12. Data from RPMs below 6,000 was not included due to the limited sensitivity of the instrument used to measure thrust.

Table 3: Recorded values of RPM and thrust, calculated C_T for static thrust tests

RPM	Thrust (N)	C_T
6082	1.23	0.1040
7081	1.75	0.1094
8000	2.28	0.1119
8952	2.90	0.1133
10479	3.99	0.1139
11331	4.70	0.1147
11852	5.20	0.1160
12308	5.58	0.1153

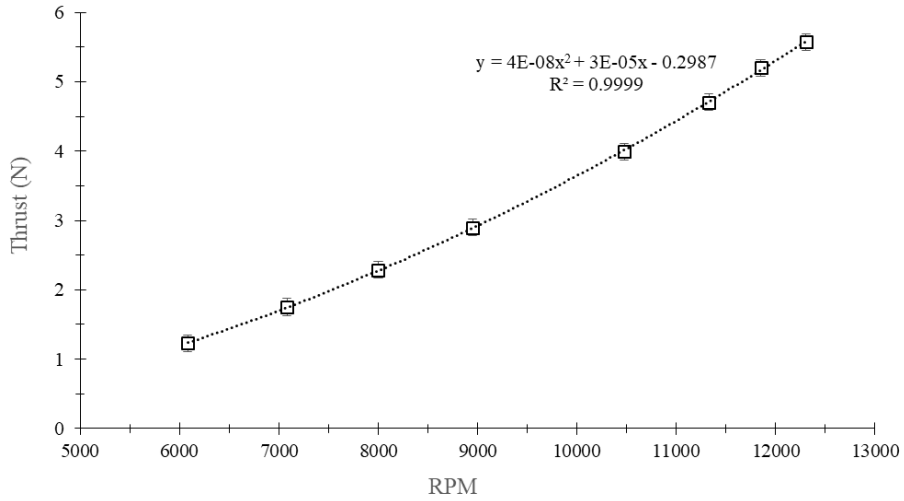


Figure 12: Measured static thrust as a function of RPM

The calculated thrust coefficients for static, far-field conditions (C_{T0}) as a function of RPM are shown in Figure 12. At these conditions, the h/D is considered infinite, $J = 0$, and $\mu = 0$. The values scale linearly with RPM with a small, positive slope (2.68 percent per 1,000 RPM). This is comparable to what is observed in the C_{T0} curves of other propellers at similar Reynolds numbers tested in previous experiments performed by Brandt (2005) and Deters et al. (2014).

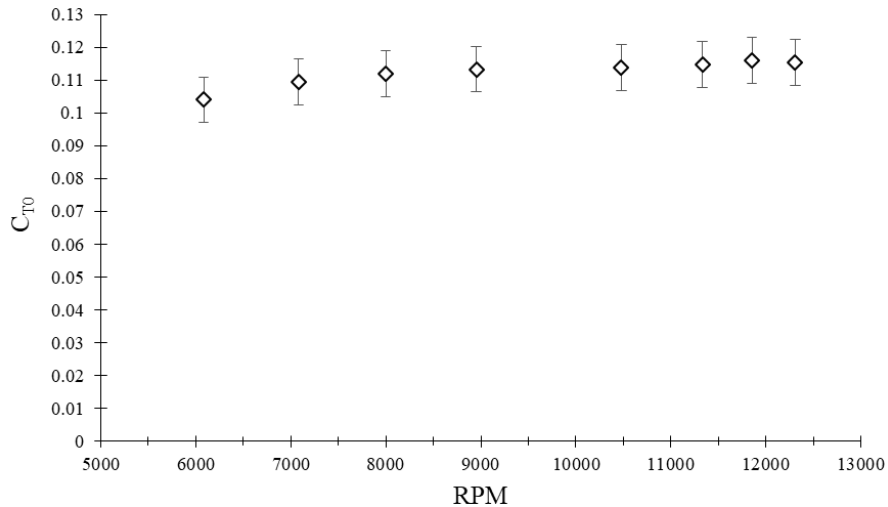


Figure 13: Static, far-field thrust coefficient as a function of RPM

The C_T curves in the ground effect experiments showed similar qualitative relationships to RPM, with lower Reynolds numbers still resulting in reductions in propeller performance. However, the wall proximity had a non-negligible impact on the production of thrust, seen below in Figure 14. For a constant RPM, decreasing the distance between the prop disk and the wall increased the thrust coefficient. At approximately 10,000 RPM and $h/D = 0.57$ (a distance of 4in), C_T increased by seven percent from C_T in the far-field. This effect stems from the impact of the wall on the vortices shed by the blades as they rotate and will be investigated further in the computational portion of this thesis. The effect of wall proximity becomes negligible at $h/D > 1.14$ ($h = 8$ in). The effect of ground proximity at 10,000 RPM is compared to data from Cai et al. (2019) in Figure 15. The increases C_T experienced by the DD7x4.5 at 10,000 RPM ($Re = 98,574$) compares well with that of the APC 11x5.5 at 6,000 RPM ($Re = 92,941$), with the values of C_T/C_{TOGE} (C_{TOGE} being the C_T calculated for the far-field case) lying within the uncertainty bound from the studies performed on the APC 11x4.5.

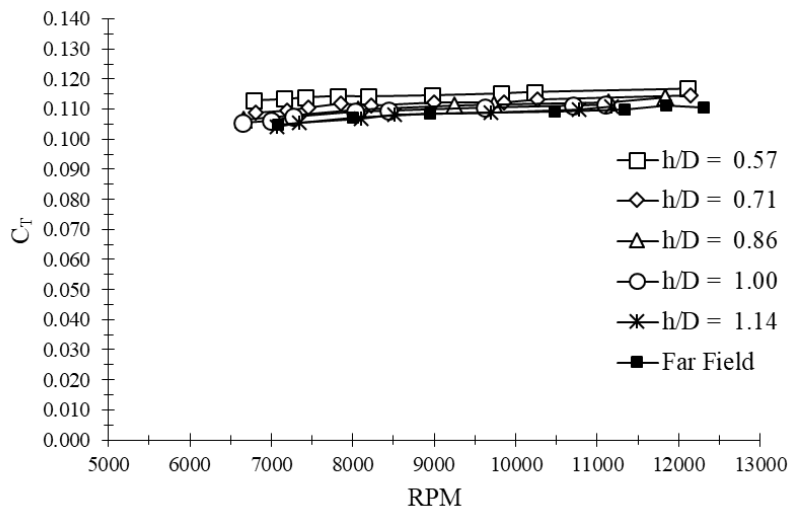


Figure 14: Coefficient of thrust vs RPM at several wall proximities

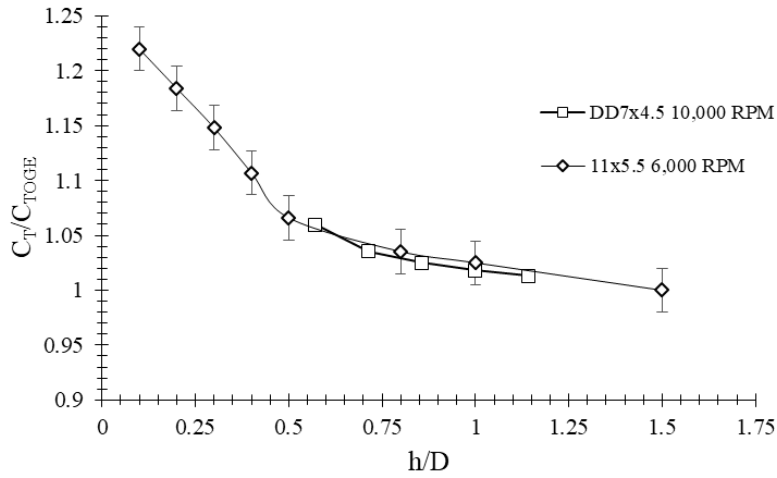


Figure 15: C_T/C_{TOGE} for the DD7x4.5 and APC 11x5.5 for a range of h/D values

The static thrust measurements and subsequently calculated C_T values were validated by comparing the known maximum ascent speed of a 1.5kg quadrotor equipped with four DD7x4.5 propellers to the theoretical maximum ascent speed possible as calculated using the thrust values from the static tests. For a 1.5kg quadrotor with four DD7x4.5 propellers, the maximum reported ascent speed was 24 m/s after a two second thrust impulse at the maximum RPM of 15,000. Neglecting drag and effects from advance ratio on the propellers' thrust during the short time interval, the maximum theoretical ascent speed can be determined using kinematics, where F_y is the force on the quadcopter in the vertical direction, T is the thrust as a function of RPM given in Figure 12, and a_y is its acceleration in the vertical direction.

$$\sum F_y = T - mg = ma_y \quad (10)$$

$$a_y = \frac{T - mg}{m} \quad (11)$$

$$V_{max} = a_y t \quad (12)$$

Substituting 1.5kg for m and 2s for t , the maximum ascent rate is predicted to be 26.0 m/s. Though this value is eight percent greater than reported, this difference is likely due to neglecting the drag

on the quadcopter and neglecting effects from advance ratio on the propeller thrust. This level of error is small enough to consider the experimental thrust measurements validated to a reasonable degree.

Uncertainties for these experiments were calculated according to procedures in Wheeler and Ganji (2010). At an RPM of 7,999, the percentage uncertainty of C_T was five percent. Values of uncertainty, mean, and standard deviation can be found below in Table 4.

Table 4: Mean, standard deviation, and uncertainties at 7,999 RPM

	Thrust (N)	RPM	C_T
Mean	2.28N	7,999	0.112
Standard Deviation	0.06N	40	-
Uncertainty	0.12N	50	0.006

Chapter V

Computational Models

The CFD simulations were run for both laminar and turbulent assumed flow. The laminar simulations allowed resolution of small-scale unsteady flow structures, while the turbulent simulations modeled small-scale fluctuations as turbulent kinetic energy. Though the low Reynolds number range of the simulations would indicate that attached boundary layers should be laminar, fluctuations are likely to arise in regions of separated flow. For this reason, both approaches were investigated.

5.1 Reynolds Averaged Navier-Stokes Modeling

The computational studies on the performance of the DD7x4.5 propeller were performed using the Reynolds-Averaged Navier-Stokes (RANS) modeling approach. The RANS approach is one of the more popular modeling approaches for both laminar and turbulent flows used in modern CFD due to its relatively low computational cost. The idea behind RANS is the concept of Reynolds decomposition, where instantaneous flow variables (e.g. velocity and pressure) are decomposed into their time-averaged and fluctuating quantities. The turbulent statistics of the flow are then evaluated using constitutive relationships in various turbulence models. The basis for the RANS approach used here is the incompressible, viscous Navier-Stokes equations for Newtonian fluids:

$$\frac{\partial \tilde{u}_i}{\partial t} + \tilde{u}_j \frac{\partial \tilde{u}_i}{\partial x_j} = -\frac{1}{\rho} \frac{\partial \tilde{p}}{\partial x_i} + \nu \frac{\partial^2 \tilde{u}_i}{\partial x_j \partial x_j} \quad (13)$$

$$\frac{\partial \tilde{u}_i}{\partial x_i} = 0 \quad (14)$$

where \tilde{u}_i is the instantaneous velocity vector and \tilde{p} is the instantaneous pressure. To obtain the RANS form of the equations, the instantaneous velocity is decomposed into the sum of its mean and fluctuating components.

$$\tilde{\mathbf{u}}(\mathbf{x}, t) = \underbrace{\overline{\mathbf{U}}(\mathbf{x})}_{\text{mean}} + \underbrace{\mathbf{u}(\mathbf{x}, t)}_{\text{fluctuating}} \quad (15)$$

In equation 14, the mean flow $\overline{\mathbf{U}}(\mathbf{x})$ is the time-averaged velocity field given by:

$$\overline{\mathbf{U}}(\mathbf{x}) = \frac{1}{\Delta t} \int_{t_0}^{t_0 + \Delta t} \tilde{\mathbf{u}}(\mathbf{x}, t) dt \quad (16)$$

This is then substituted back into equation 13. The resulting equations are then ensemble-averaged, resulting in the RANS equations:

$$\frac{\partial \overline{u}_i}{\partial t} + \overline{U}_j \frac{\partial \overline{u}_i}{\partial x_j} = -\frac{1}{\rho} \frac{\partial \overline{p}}{\partial x_i} + \nu \frac{\partial^2 \overline{u}_i}{\partial x_j \partial x_j} - \underbrace{\frac{\partial \overline{u_j u_i}}{\partial x_j}}_{\text{Reynolds Stress}} \quad (17)$$

Ensemble-averaged quantities are denoted by an overbar. Due to the Reynolds decomposition, the resulting equations are unclosed, as there are four equations with 10 unknowns. The Reynolds stress transport equation can be derived from equations 15 and 17:

$$\begin{aligned} \frac{\partial \overline{u_i u_j}}{\partial t} + \overline{U}_k \frac{\partial}{\partial x_k} \overline{u_j u_i} = & -\frac{1}{\rho} \underbrace{\left(\frac{\partial}{\partial x_i} \overline{u_j p} - \frac{\partial}{\partial x_j} \overline{u_i p} \right)}_{\text{Redistribution}} - 2\nu \underbrace{\left(\frac{\partial}{\partial x_k} \overline{u_i} \frac{\partial}{\partial x_k} \overline{u_j} \right)}_{\text{Dissipation}} \\ & - \underbrace{\frac{\partial}{\partial x_k} \overline{u_k u_i u_j}}_{\text{Turbulent Transport}} - \underbrace{\overline{u_j u_k} \frac{\partial}{\partial x_k} \overline{U}_i - \overline{u_i u_k} \frac{\partial}{\partial x_k} \overline{U}_j}_{\text{Production}} + \underbrace{\nu \frac{\partial^2}{\partial x^2} \overline{u_i u_j}}_{\text{Molecular Viscous Transport}} \end{aligned} \quad (18)$$

The equation for turbulent kinetic energy can be obtained by contraction of equation 18:

$$\frac{\partial k}{\partial t} + \overline{U}_k \frac{\partial k}{\partial x_k} = \underbrace{-\frac{1}{\rho} \frac{\partial}{\partial x_i} \overline{u_i p}}_{\text{Pressure Diffusion}} - \underbrace{\nu \frac{\partial \overline{u_i} \partial \overline{u_i}}{\partial x_k \partial x_k}}_{\text{Dissipation}} - \underbrace{\frac{1}{2} \frac{\partial}{\partial x_k} \overline{u_k u_i u_i}}_{\text{Turbulent Transport}} - \underbrace{\overline{u_i u_k} \frac{\partial}{\partial x_k} \overline{U}_i}_{\text{Production}} + \nu \frac{\partial^2}{\partial x^2} k \quad (19)$$

where $k \equiv \frac{1}{2} \overline{u_i u_i}$. The annotated portions of equation 19 will be briefly explained.

Dissipation is the decay of turbulence in a flow field due to the viscous damping at small length scales. Turbulent transport is the transport of turbulent kinetic energy due to the fluctuations of turbulent velocity. Pressure diffusion is the transport of turbulent kinetic energy in space due to fluctuations in pressure. The production term represents the rate that the kinetic energy from the mean flow field is transferred to turbulent fluctuations in the flow field. Convective transport, pressure diffusion, and turbulent transport are conservative, as they serve only to move turbulent kinetic energy from one location to another. Dissipation and production are non-conservative, and represent a sink and source term, respectively. Equation 19 is the basis of the turbulence models used in this study: standard k - ϵ (Jones and Launder, 1972), shear stress transport- k - ω (Menter, 1994), and transitional k - k_t - ω (Walters and Cokljat, 2008).

Chapter VI

CFD Case Setups

6.1 Propeller Geometry

The aforementioned DD7x4.5 propeller was investigated in this study. The 7x4.5 is typically used in small fixed wing UAVs or Class-I quadrotors in the 1.5kg size range. To generate an accurate digital geometry of the propeller for the creation of a mesh, a physical copy of the DD7x4.5 was sent to Arrival3D scanning services in Oklahoma City, OK. The propeller was scanned using a laser three-dimensional scanner with a rated accuracy of 0.001in. The resulting point cloud was turned into an IGS file, seen below in Figure 16. The geometry of the motor and quadrotor structure was not included in the simulations.

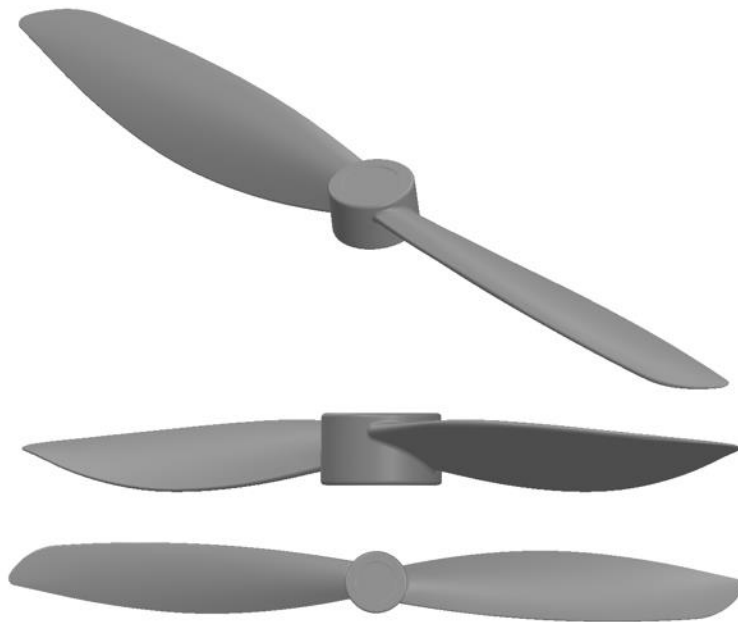


Figure 16: DD7x4.5 digital geometry used in the CFD studies

6.2 Mesh Generation

The far-field boundary of the computational domain was placed at $2.57D$ from the center of the propeller in the radial direction. The top boundary was placed $1.07D$ upstream of the propeller disk, while the bottom boundary was placed $2D$ downstream of the propeller disk. The domain is shown in Figure 17:

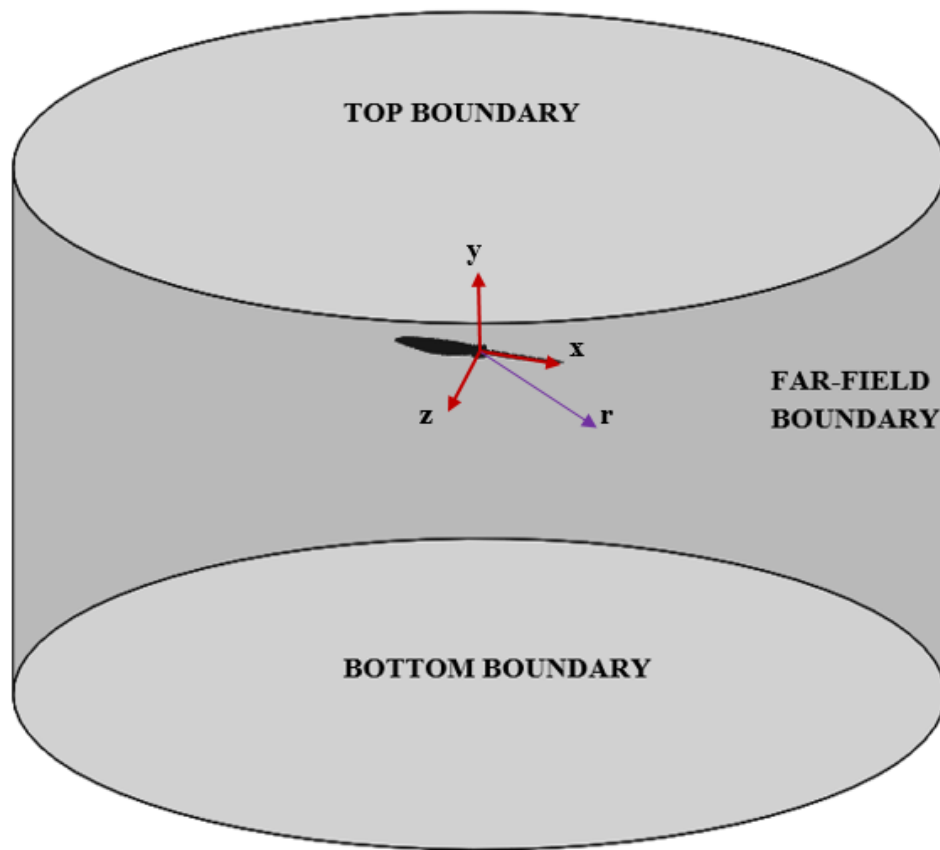


Figure 17: Computational domain boundaries with propeller shown within the domain

Kutty and Rajendran (2017) showed that a mesh size of 4×10^6 cells is sufficiently refined for the simulation of low Reynolds number propellers using a second order discretization scheme. For the current study, the mesh used consisted of 1.3×10^7 cells of triangular and quadrilateral types. The mesh consisted of tetrahedral elements in the far field and triangular prism elements near the blade surface. Due to the mesh being an order of magnitude larger than that seen in

comparable studies, and because of the lack of convergence issues using second-order schemes, the mesh was assumed to be sufficiently refined. Figure 18 shows the grid near the propeller's surface at a span-wise location of $0.5R$. The prism layer of cells can be seen near the airfoil surface, which allows for steep gradients in the wall-normal direction to be resolved accurately.

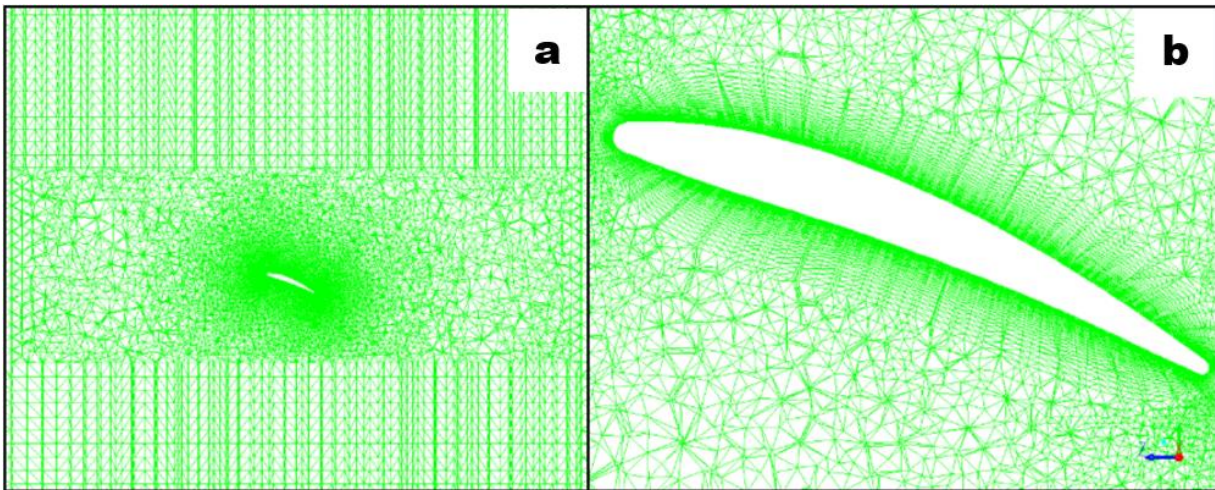


Figure 18: (a-b) Structured and unstructured meshes near propeller blade at span $0.7R$

6.3 Boundary Conditions

Several different types of boundary conditions were employed within FLUENT during the CFD simulations. These different types are explained below:

- Pressure Inlet: Boundary cells are assigned a gauge pressure (0 Pa). If the flow is turbulent, values of turbulent kinetic energy and dissipation rate/specific disputation rate must be known. This type of boundary can be used when no flow rate is known, as is true for the top boundary.
- Pressure Outlet: Outflow conditions at boundary cells are calculated using the assigned gauge pressure at the outlet (0 Pa). Flow velocities can be calculated based on fluxes. All

velocity gradients are fixed to zero. All unknown quantities (including turbulent quantities) are calculated from the interior of the domain.

- Symmetry: Boundary cells are assumed to have a velocity normal to the cell face of zero. Gradients of velocity, pressure, and turbulent quantities normal to the cell face are also assumed to be zero.
- Velocity Inlet: Boundary cells are assigned a non-zero mean velocity in the x, y, or z-directions.
- Wall: Velocity at the cell face is equal to zero, per the no-slip condition.

In the simulations, the propeller geometry was always assigned a wall boundary condition, while the boundary cells were assigned various boundary conditions based on the parameters being studied. This made for two unique boundary conditions for each simulation.

6.3.1 Static Cases

For the static, far-field cases, the top boundary was set as a pressure inlet, with the bottom boundary being set as a pressure outlet at standard atmospheric pressure. The far-field boundaries in the radial direction were set as symmetry boundaries.

6.3.2 Advancing and Crosswind Cases

For cases where the propeller is ascending or descending, all boundaries were prescribed with constant mean velocities in the y-direction within the simulation. When turbulence models were employed, values for turbulent kinetic energy (k), turbulent dissipation rate (ϵ), and specific dissipation rate (ω_s) were calculated using an assumed turbulence intensity (I) of 0.1 percent and assumed viscosity ratio of 10 (Kutty and Rajendran, 2017) and assigned to all boundaries and

initialized for the entire flow field. The equations used to calculate turbulent kinetic energy, turbulent dissipation rate, and specific dissipation rate are respectively presented below.

$$k = \frac{((\Omega R)l)^2}{2/3} \quad (20)$$

$$\varepsilon = \frac{0.09k^2}{10\nu} \quad (21)$$

$$\omega_s = \frac{k}{10\nu} \quad (22)$$

Crosswind cases used similar boundary conditions, with all boundary cells assigned a constant mean velocity in the z-direction within the simulation. The initial conditions were to assign all cells within the simulation domain with the same mean velocity as used by the boundary cells.

6.3.3 Ground Effect Cases

Cases studying the effect of ground proximity were performed by changing sets of points set as interior points to walls. Sets of these points were placed within the grid at 2in, 3in, 4in, 5in, 6in, 7in, 8in, 9in, 10in, 11in, and 12in from the propeller disk. For example: when simulating ground effect at $h = 6\text{in}$, the set of interior points at $h = 6\text{in}$ would be fixed as a wall boundary, while all other points would remain as interior points. The top and far-field boundaries were set as symmetry boundaries. The sets of points used as wall boundaries can be seen at $h = 4\text{in}$, $h = 6\text{in}$, $h = 8\text{in}$, $h = 10\text{in}$, and $h = 12\text{in}$ below in Figure 19.

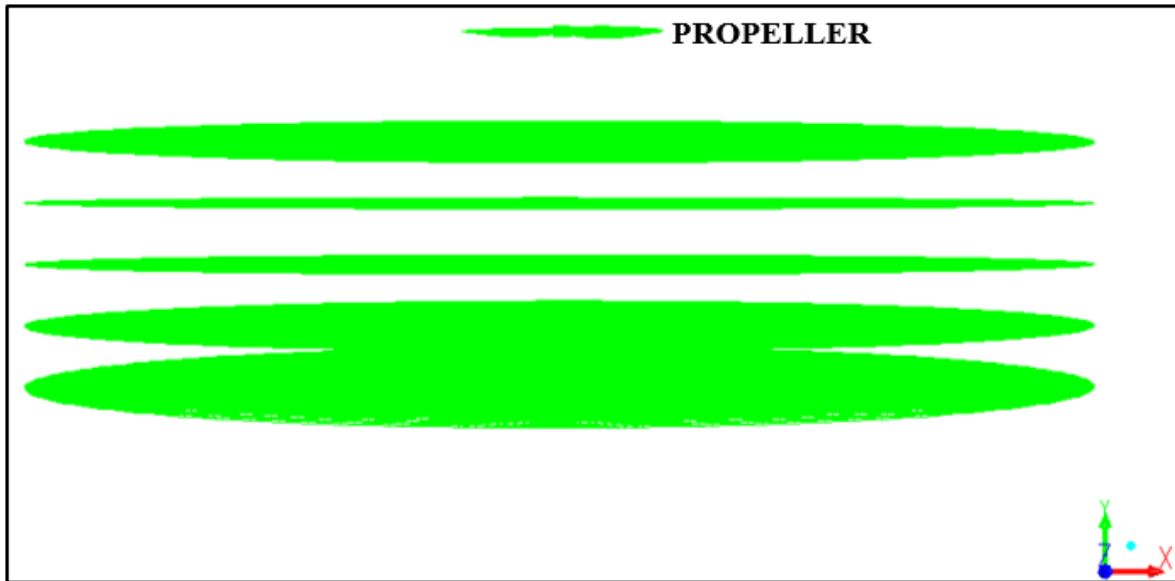


Figure 19: Groups of cells used as wall boundaries in ground effect simulations

6.4 Numerical Methods

All simulations were performed using the pressure-based solver in Ansys FLUENT-v16.2. The numerical scheme used depended on whether the problem was solved as a steady state case or as a transient case. Details are provided below.

For all cases, a second-order upwinding scheme was used for the convective terms of the transport equations (Barth and Jespersen, 1989). The pressure terms were discretized using a scheme in which the pressure on the face of each cell was obtained from the average of the pressure values in the neighboring cells. The SIMPLE scheme was used for pressure-velocity coupling (Patankar and Spalding, 1972). The calculated thrust reported from the simulations was the total force in the y-direction generated exerted on the propeller. This force will be a sum of two components: force due to pressure differences, and force due to viscous effects from wall shear. This calculation was performed automatically by the FLUENT software and is detailed in the

equation below, with the integrations being performed around the entirety of the propeller's surface and \hat{n} being the unit vector normal to the propeller blade surface.

$$T = F_y = \underbrace{\oint P \hat{n} dA}_{\text{Pressure Component}} + \underbrace{\oint \tau_w dA}_{\text{Viscous Component}} \quad (23)$$

For the static cases, advancing cases, and ground effect cases, the simulations were run as steady-state problems with the fluid domain being rotated around the static propeller. Due to the inherent unsteadiness in some parts of the flow field, small oscillations in the reported thrust were observed. Due to this unsteadiness, averages were taken of the calculated thrust values over 1,000 iterations once the changes in thrust from the previous iteration fell below one percent. Figure 20 shows plots of the thrust values for four different cases run at an RPM of 10,000: the static case, $J = 0.375$, $J = 0.5$, and $h = 4\text{in}$. The portion of the simulations past which the averages were taken is denoted with a red line.

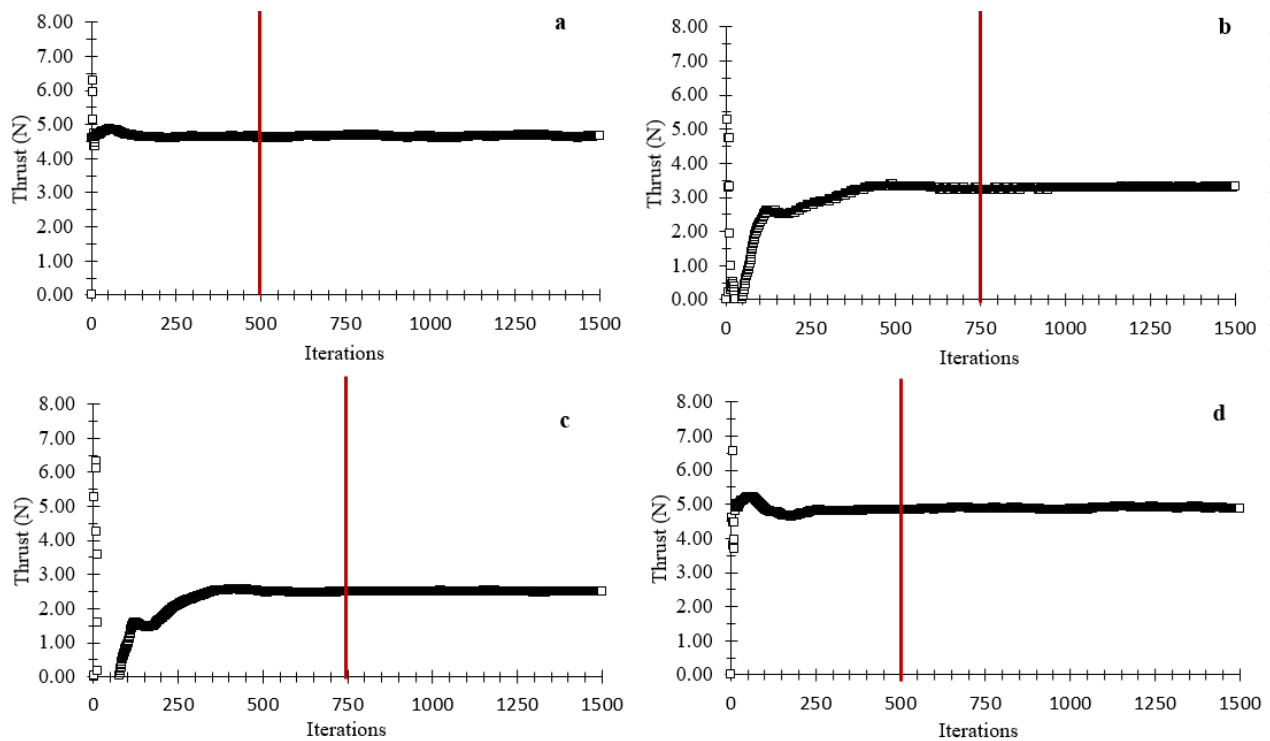


Figure 20: Thrust convergence at 10,000RPM, a.) Static b.) $J = 0.375$ c.) $J = 0.50$ d.) $h = 4\text{in}$

The initial 50 iterations of each of the simulations exhibited high-amplitude unsteady thrust oscillations. For the static cases, 1,500 iterations were sufficient to produce adequate convergence with the exception of the lower RPM range (1,000-3,000 RPM). These required 2,000 iterations. For the advancing cases and ground effect cases, 1,500 iterations were sufficient regardless of RPM. Thrust convergence at 10,000 RPM at $J = 1.0$, $J = 0.875$, $J = 0.75$, $J = 0.625$, $J = 0.50$, $J = 0.375$, $J = 0.25$, and $J = 0.125$ is shown below in Figure 21.

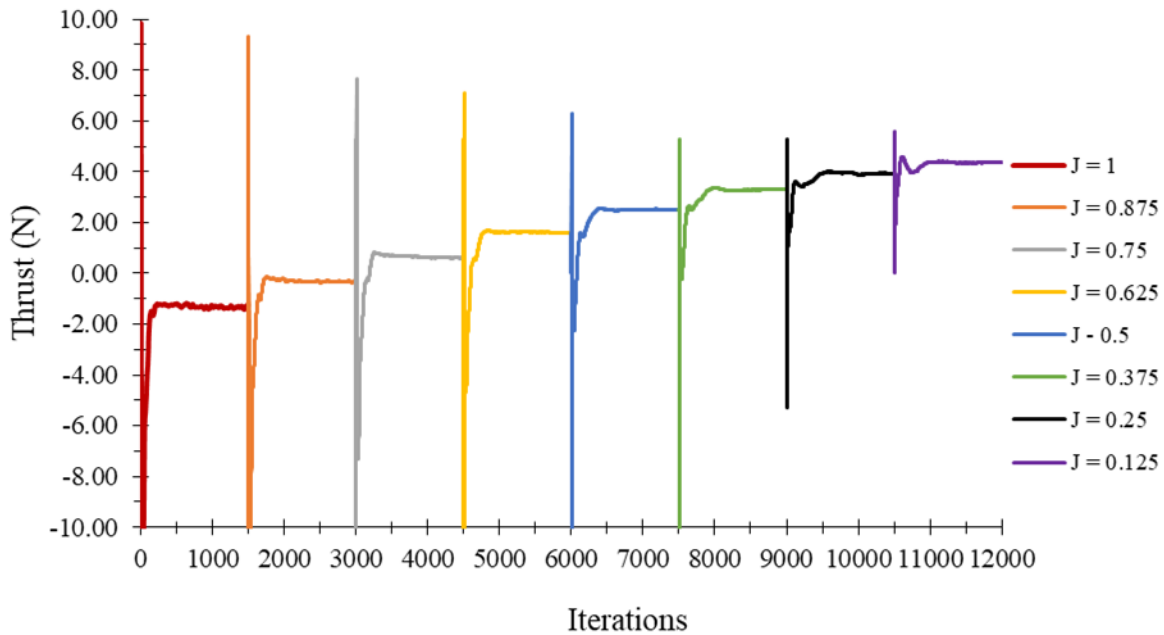


Figure 21: Thrust convergence at 10,000 RPM over a range of advance ratios

For the crosswind cases, the steady-state assumption could no longer be used. This is due to the fact that the wind vector as viewed in a reference frame attached to the blades is changing as the blades rotate. It was therefore necessary to run the crosswind simulations as transient cases. These cases were run with a moving mesh rather than a moving reference frame. For all cases, the number of time steps per blade rotation was held constant at 360 with 20 iterations per time step. The simulations were performed over a period of five blade rotations, or 1,800 time steps. Second-order implicit time stepping was used in all transient cases. Transient cases were considered

converged when the amplitude of the thrust oscillations throughout one blade rotation remained within one percent of the amplitude from the previous rotation. The thrust value reported for each case was the average thrust over a period of one blade rotation after convergence. Figure 22 shows how thrust varies throughout the blades rotation.

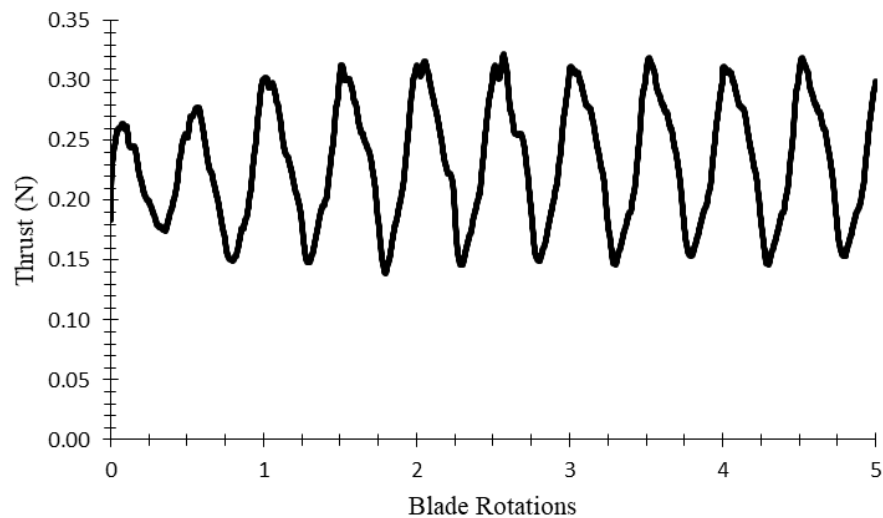


Figure 22: Thrust over a period of five blade rotations at 2000 RPM, $\mu = 0.25$

6.5 Computational Requirements

Due to the large size of the mesh used (1.3×10^7 cells), the use of high-performance computing (HPC) resources was a necessity. The HPC utilized were provided by the University of Oklahoma Supercomputing Center for Education and Research (OSKER). Each simulation required a minimum of two computing nodes. Each node consisted of 20 CPU cores with 32GB RAM. With two nodes, the steady state simulations were completed in 1-2 hours of runtime for each individual case. Transient simulations required four nodes, and each case was completed with between 14-15 hours of runtime.

Chapter VII

CFD Results

In the chapter, results from the CFD simulations are presented. Data from test cases that demonstrate the impacts of boundary conditions, steady-state vs transient simulations, and laminar vs turbulent simulations are given. Results for static thrust performance and thrust performance in ground effect are compared to the experimental data from chapter IV. Visual references that seek to explain the flow physics behind the thrust trends are presented alongside the thrust results. The goal is not only to build an empirical model from the results presented, but also to demonstrate that the simulations are accurately capturing the physics of the propeller flow field. The CFD results showed good qualitative agreement with the previously performed experimental data, with the CFD results consistently biased to higher thrust values compared to experimental measurements. This bias error is likely partially due to the simulations being run as laminar simulations when the flow field has small amounts of turbulence and partially due to the simulations using a propeller that was simply spinning in space with no obstructions from mounting equipment. It was shown that laminar and turbulent simulations captured trends of thrust production with equal effectiveness, allowing for results from laminar simulations to be anchored by the experimental data.

7.1 Test Cases

Several test cases were run to study the impact of different boundary conditions, transient vs steady state cases, and laminar vs turbulent cases on the results of the simulations. The boundary condition and transient vs steady state studies were performed in order to ensure results from static cases, advancing cases, crosswind cases, and ground effect cases could be viewed without need

for adjustments. Cases employing turbulence models were run to ensure that cases run as laminar simulations captured trends equally as well as turbulent simulations.

7.1.1 Boundary Condition Tests

Three different sets of boundary conditions were tested at an RPM of 10,000 in static conditions: those used for static cases, those used for advancing/crosswind cases, and those used for ground effect cases. These boundary conditions are detailed in 6.3. The results of these tests are detailed below in Table 5.

Table 5: Impact of boundary conditions on thrust production at 10,000 RPM

Case Type	Boundary Conditions	Thrust (N)
Static Case	Top: Pressure Inlet Bottom: Pressure Outlet Far Field: Symmetry	4.652
Advancing/Crosswind	All boundaries as velocity inlets	4.652
Ground Effect	All boundaries as symmetry except for wall at $h = 12\text{in}$	4.653

This test demonstrated that the type of boundary condition employed had negligible impact on the thrust values reported and that the computational domain used was sufficient in size.

7.1.2 Transient vs Steady State

Due to crosswind cases employing a transient solver, it was necessary to investigate the impact of the unsteady terms on the reported thrust from a static case at 10,000 RPM. These test cases were used to study the differences in thrust prediction between steady-state and transient cases, as well as the impact of reference frame motion vs mesh motion. While the steady-state test case employed a moving reference frame analogous to the static, advancing, and ground effect cases, the first transient test case employed a dynamic mesh. A second transient test case was also

run using a moving reference frame instead of a dynamic mesh. The results of the test are given in Table 6.

Table 6: Static thrust at 10,000 RPM for steady-state and transient simulations

Case Type	Thrust (N)	Difference (%)
Steady-State (Moving Reference Frame)	4.65	-
Transient (Moving Reference Frame)	4.54	-2.36
Transient (Moving Mesh)	4.55	-2.15

The test cases showed a small difference of just over two percent between steady-state and transient thrust predictions at the same operating conditions. The discrepancy can be explained by looking at contours of relative velocity magnitude (RVM) and examining the behavior of the boundary layer between the steady state and transient cases. RVM refers to the magnitude of the velocity relative to the propeller blade surface (e.g., zero at the blade surface due to the no-slip condition). Figure 23 showcases two plots of RVM at 10,000 RPM: the first from the steady state case, and the other from the time-averaged, transient case. The time-averaged RVM contour shows a significant amount of open flow separation along the suction side when compared with the instantaneous, steady state case. The boundary layer is observed to separate, then reattach in the steady state case, while the separation remains open in the time averaged case.

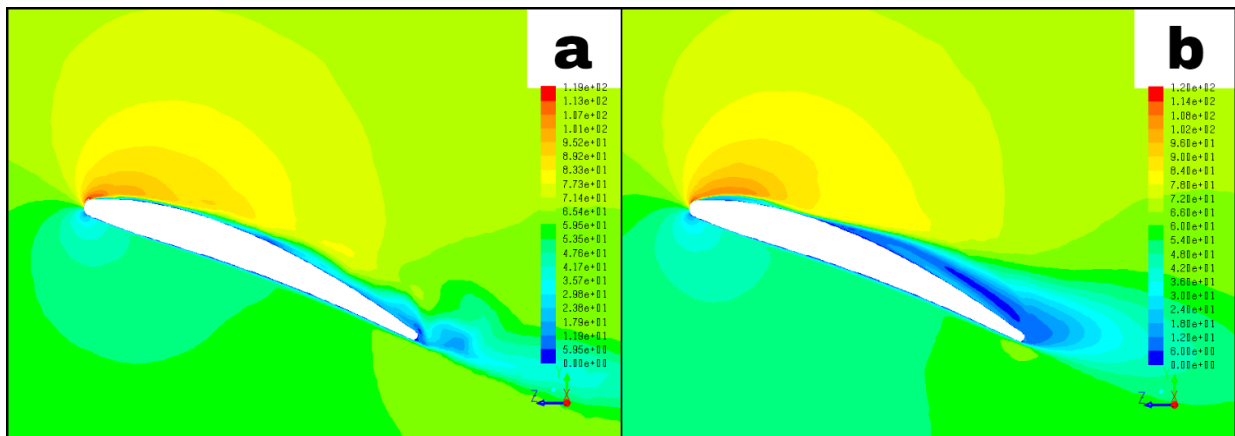


Figure 23: RVM Contours at span 0.7R at 10,000 RPM, a.) Instantaneous b.) Time-Averaged

The impact of this differing boundary layer behavior on thrust production is reflected in the plots of coefficient of pressure along the blade's surface. Pressure coefficient is defined as:

$$C_P = \frac{p - p_\infty}{q_\infty} \quad (24)$$

where p is the local static pressure, p_∞ is the far field atmospheric pressure, and q_∞ is the far field dynamic pressure. In Figure 24, s/c represents the chord-wise location along the blade section. Near the leading edge, C_P is noticeably reduced on the suction side in the time-averaged case vs that of the instantaneous, steady state case. The addition of the unsteady term also has the effect of flattening the shape of the C_P curve in the area of $s/c = 0.1$ before the flow separates at $s/c = 0.2$. It can therefore be concluded that the addition of the unsteady term to the simulation is responsible for the small discrepancy in thrust production, as the variation in thrust production between the transient case with the moving mesh and the transient case with a moving reference frame was negligible. Since the final empirical thrust model will use the experimental data as anchor points for the CFD data, this difference can be taken into account for both steady-state and transient CFD results. The decision to neglect this small discrepancy was also influenced by computational cost, as steady state simulations could be performed at a rate 10-15 times higher than transient simulations and could produce nearly identical computational performance.

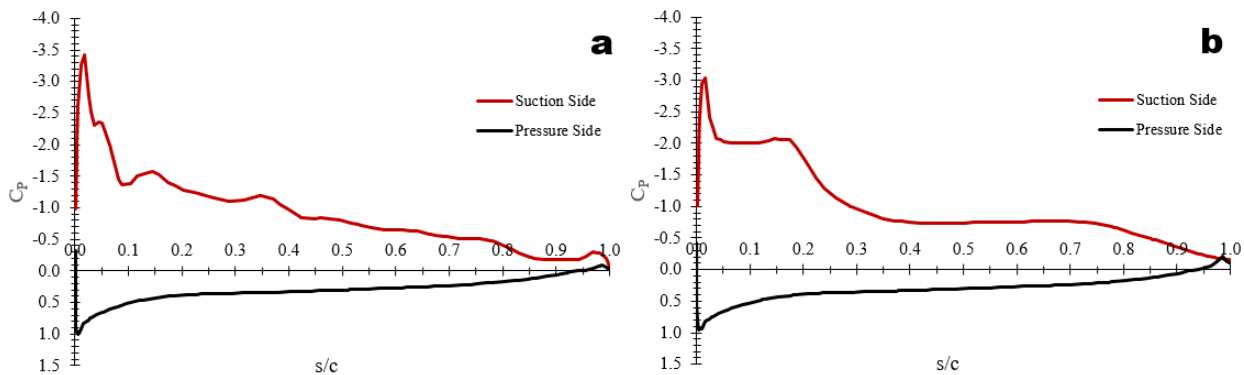


Figure 24: C_P vs s/c at span 0.7R, 10,000 RPM a.) Instantaneous b.) Time-Averaged

7.1.3 Turbulent vs Laminar

A series of cases were run comparing the performance of three different turbulence models in capturing the trends of thrust production across a range of axial advance ratios. The three models that were used were the standard $k-\epsilon$ model, the SST- $k-\omega$ model, and the $k-k_1-\omega$ transition model. These were compared to the laminar simulations run without a turbulence model. The simulations for these test cases were run at an RPM of 10,000. The results of these tests can be seen in Figure 25.

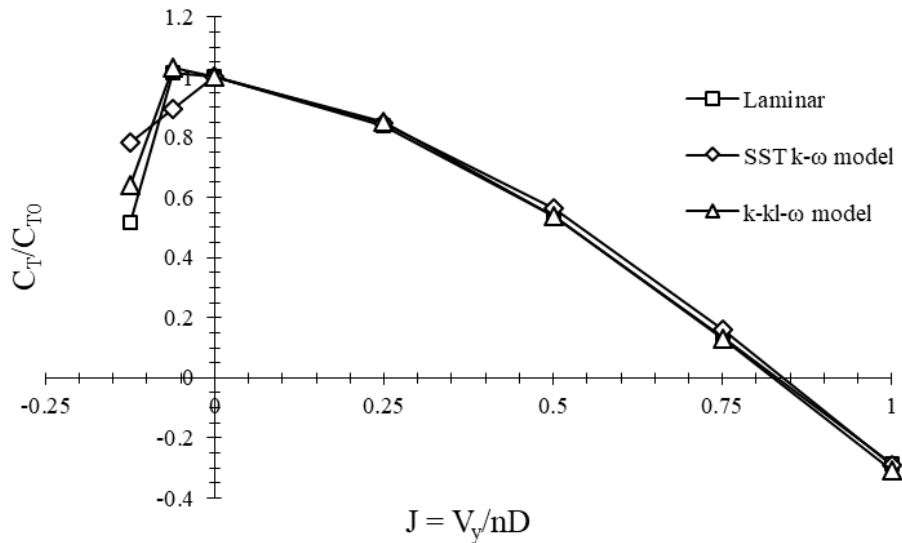


Figure 25: Ratio of C_T to C_{T0} vs J at 10,000 RPM using several turbulence models

Simulations using the standard $k-\epsilon$ model did not converge at any advance ratio. This poor performance can be attributed to the $k-\epsilon$ model's underlying mathematics and assumptions, which are not designed with low-Reynolds number or transitional flow in mind. The $k-\epsilon$ model assumes the entire boundary layer is turbulent from the stagnation point onwards regardless of whether this is true in reality. The other two models tested, the SST- $k-\omega$ model and the $k-k_1-\omega$ transition model, performed similarly to the laminar model at positive advance ratios. The $k-k_1-\omega$ transition model

produced similar results to the laminar simulation for negative advance ratios where the blades are experiencing the onset of stall. Due to the $k-k_l-\omega$ transition model's ability to model the boundary layer as laminar in some locations and turbulent in others, it does not artificially delay flow separation as done by the standard $k-\epsilon$ model and the SST- $k-\omega$ model. Because of the inherent modeling errors present in turbulence models, the presence of convergence issues, and the lack of any improvement in computational accuracy in modeling thrust trends, the remainder of the cases in this study were run as laminar simulations. The laminar simulations, due to the fine grid used, were actually able to resolve some scales of turbulence in the flow field, analogous to the modeling technique known as implicit large-eddy-simulation.

7.2 Static Cases

The CFD simulations for static thrust performance produced results that were qualitatively similar to the experimental results from chapter IV. Static thrust performance degraded at Reynolds numbers below 10,000 (RPM <3,000) due to separation and recirculation within the boundary layer. Static thrust coefficient as computed from CFD is plotted below in Figure 26 and compared with the experimental values from section 4.3. Table 7 presents the conversion between RPM and Reynolds number for ease of comparison.

Table 7: Conversion between RPM and Re at 75 percent span

RPM	Re
1000	7,393
2000	14,786
3000	22,179
4000	29,572
5000	36,965
6000	44,359
7000	51,752
8000	59,145
9000	66,538
10000	73,931
11000	81,324
12000	88,717
13000	96,110
14000	103,503
15000	110,896

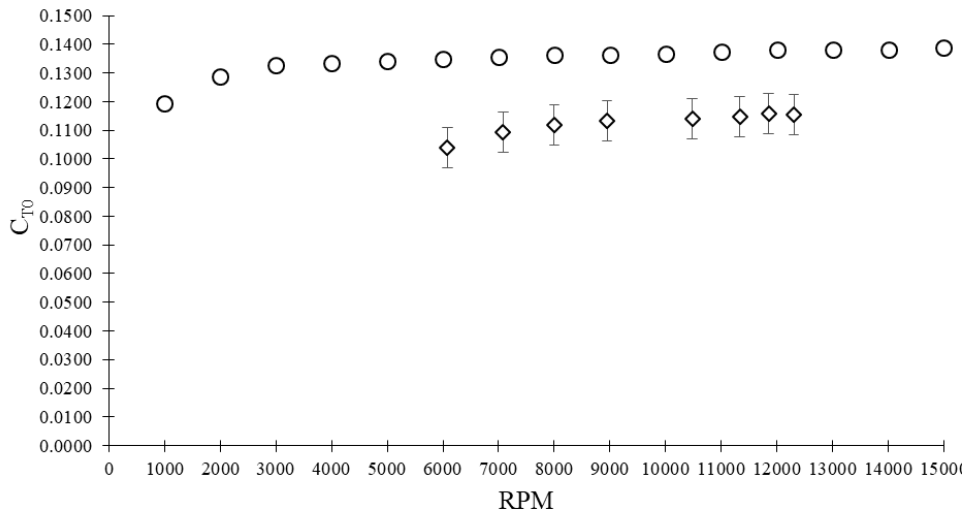


Figure 26: Static thrust coefficient vs RPM from CFD and experimental measurement

The results from CFD show a consistent 20 percent bias error in the curve for C_{T0} . The qualitative shape of the curve is consistent with those seen in experimental measurements presented by Brandt (2005) and Deters et al. (2014), with a slow linear increase in C_{T0} with increasing RPM (one percent for every 1,000 RPM). The effects on C_{T0} from increasing RPM (and

by extension, Re) can be easily seen in the contours of relative velocity magnitude (RVM) at several RPMs in Figure 27. At 1,000 RPM (local section $Re = 6,721$), the boundary layer experiences significant separation and recirculation along the aft portion of the blade. The wake at this RPM is also significantly larger than that seen at higher RPMs. At 5,000 RPM (local section $Re = 33,605$), this separation has for the most part closed, with significant recirculation along the trailing edge having disappeared. Laminar separation bubbles can still be seen along the suction side of the blade section, and separation and unsteadiness can be observed along the trailing edge. At 10,000 RPM (local section $Re = 67,208$) and 15,000 RPM (local section $Re = 100,812$), the boundary layer has significantly thinned, with less evidence of laminar separation bubbles. Separation and unsteadiness can still be observed along the trailing edge.

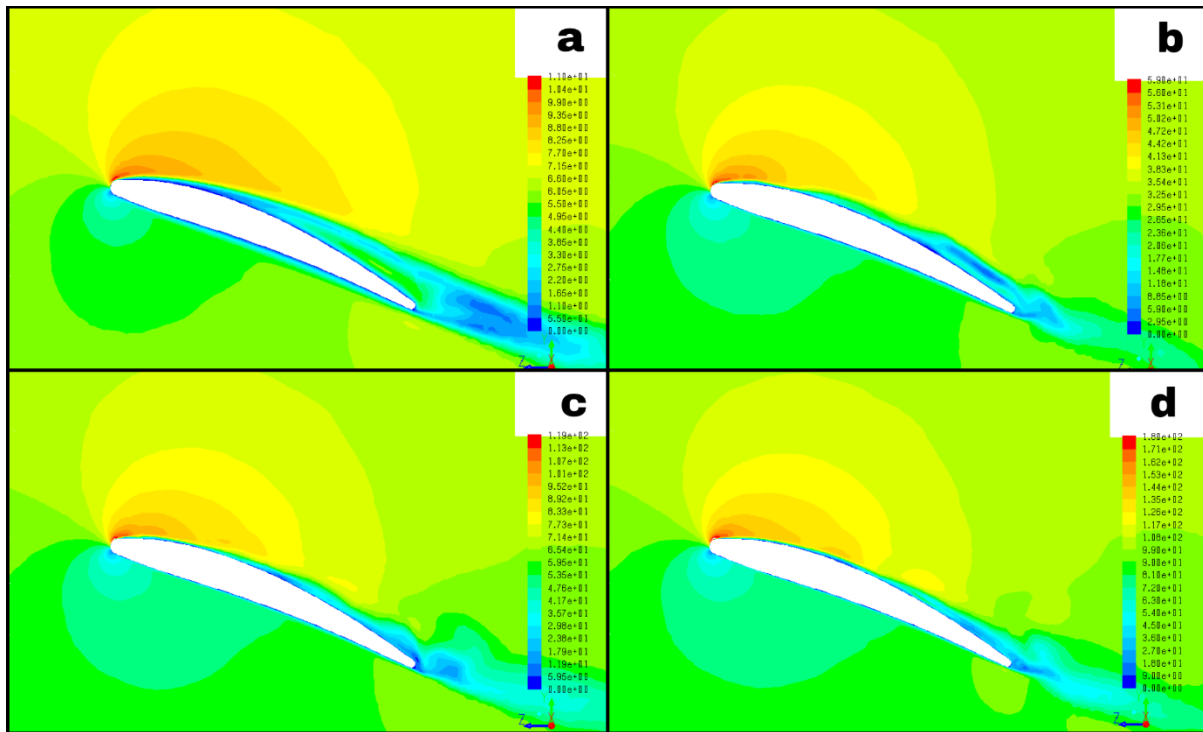


Figure 27: RVM contours at span 0.7R a.) 1,000RPM b.) 5,000RPM c.) 10,000RPM d.) 15,000RPM

The effects of these differences in boundary behavior on thrust production are reflected by the distribution of coefficient of pressure along the blade section's surface in Figures 28 and 29. At 1,000 RPM, there is little evidence of unsteadiness along the length of the blade section, and the peak C_P magnitude near the leading edge on the suction side is markedly reduced when compared to the peak suction side C_P magnitude at 5,000, 10,000, and 15,000 RPM. This reduction is directly responsible for the poor static performance of the propeller at low RPMs. As RPM increases, the peak suction side C_P increases gradually, analogous to the gradual linear increase in C_{T0} seen in Figure 24. Increased unsteadiness is also seen along the airfoil section with increasing RPM as the boundary layer separates and then reattaches near the trailing edge of the blade.

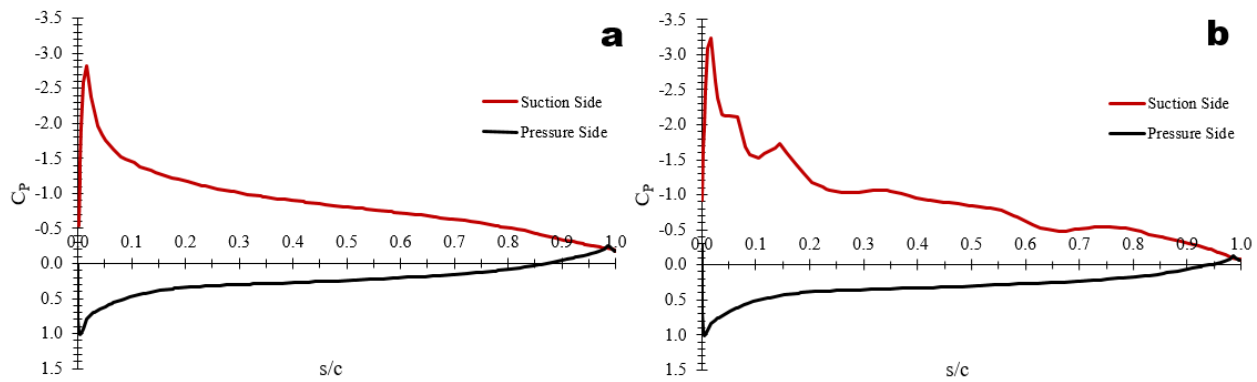


Figure 28: C_P vs s/c at span 0.7R, a.) 1,000 RPM b.) 5,000 RPM

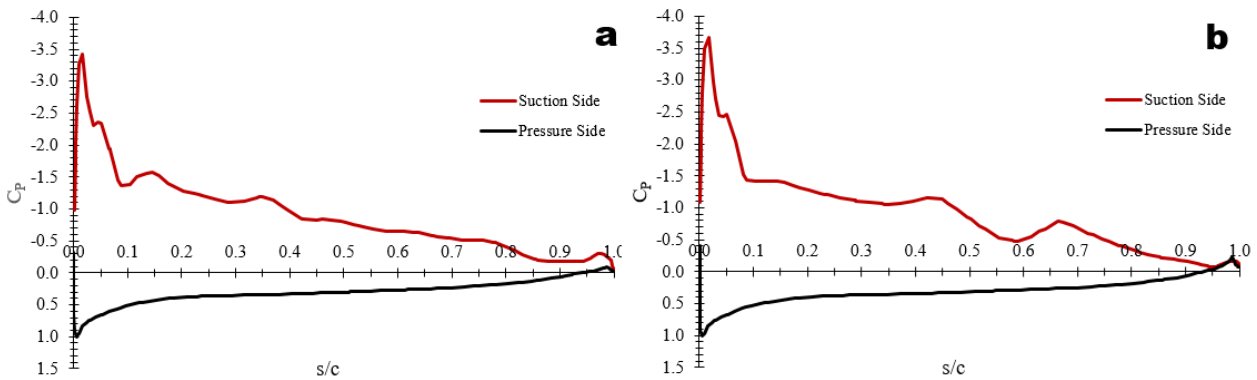


Figure 29: C_P vs s/c at span 0.7R, a.) 10,000 RPM b.) 15,000 RPM

The impact of Reynolds number can also be seen on the distribution of wall shear stress on the propeller blades themselves. In general, wall shear stress is proportional to the velocity gradient within the boundary layer. As Reynolds number increases, the growth of shear stress along the propeller blade surface is limited. This can be seen in the contours of wall shear stress on the suction side of the blade in Figure 30.

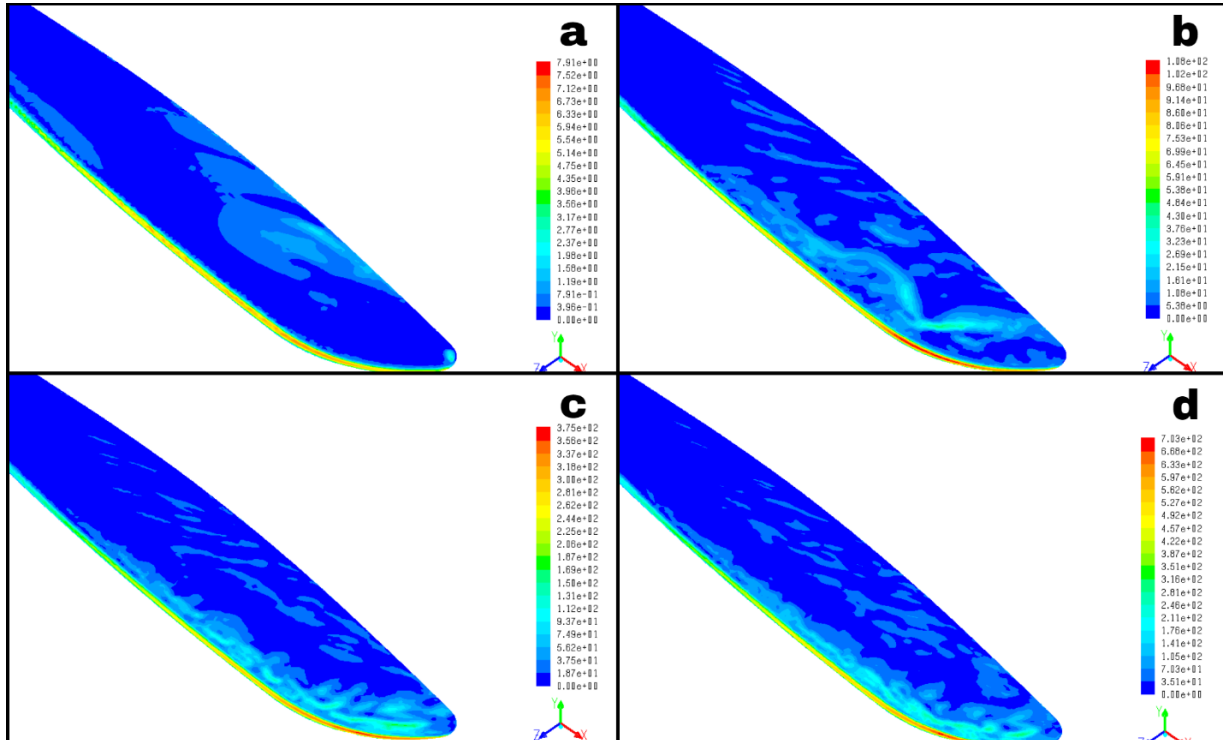


Figure 30: Contours of wall shear stress on the blade suction side a.) 1,000RPM b.) 5,000RPM c.) 10,000RPM d.) 15,000RPM

For accurate comparison of the shear stress distribution at multiple RPM's, the non-dimensional coefficient of friction is defined as:

$$C_f = \frac{\tau_w}{q_\infty} \quad (25)$$

where τ_w is the wall shear stress on the propeller blade and q_∞ is the freestream dynamic pressure.

The coefficient of friction was plotted as a function of s/c in Figure 31. As RPM (and by extension,

Reynolds number) is increased, the shear stress grows at a smaller rate than the freestream dynamic pressure, resulting in lower values of C_f with increased RPM. At 1,000 RPM, C_f increases as s/c increases after $s/c = 0.2$ as a result of the large amounts of laminar separation and recirculation within the boundary layer. This is in contrast to the higher RPMs, where C_f stabilizes at very low values after initially being very high at the leading edge.

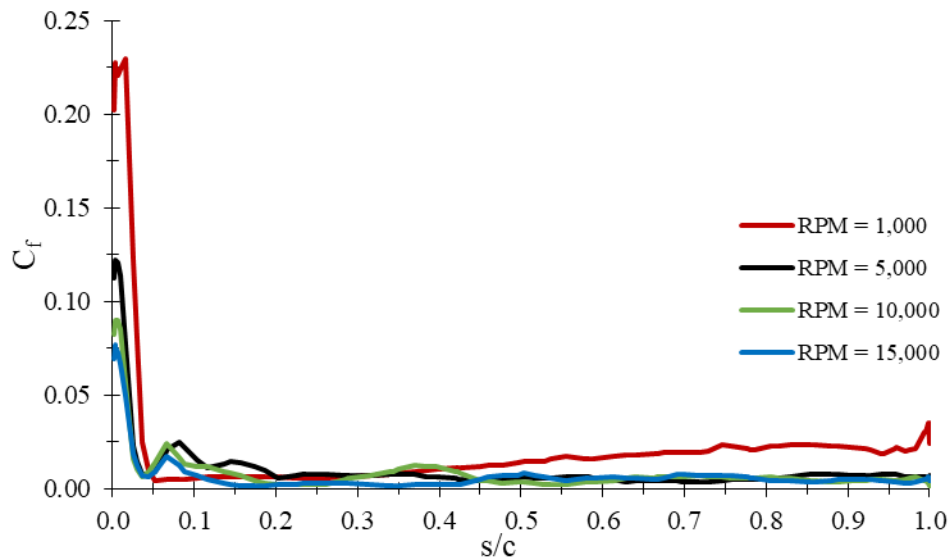


Figure 31: Friction coefficient vs s/c at span $0.7R$ at multiple RPM's.

Though C_T degrades at low Re , thrust itself still varies primarily with the square of RPM in the static case, with the effects from low Reynolds numbers mostly becoming imperceptible when compared to the effects from changing RPM. This is illustrated in Figure 32.

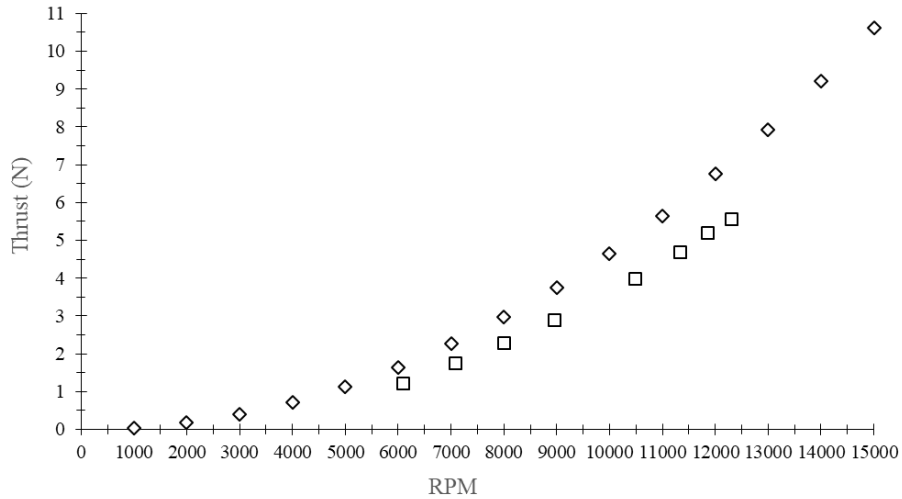


Figure 32: Static thrust vs RPM as predicted by CFD and experiments

7.3 Advancing Cases

The impact of axial advance ratio on thrust production can be separated into two classifications: ascending flight, where advance ratios are denoted as positive, and descending flight, where advance ratios are denoted as negative. The impact of advance ratio on thrust production in the ascending state is a product of decreasing aerodynamic angle of attack on the blades, while the descending state is governed both by increased thrust and stall due to increased angle of attack and thrust reduction due to the beginnings of the vortex-ring state. Thrust coefficient as a function of axial advance ratio is presented below over a range of RPMs in Figure 33. Thrust coefficients at negative advance ratios below -0.125 were not reported, as the force in the y-direction within the simulations, reported as thrust, becomes increasingly dominated by the drag generated by the descending propeller. Though the curves at each RPM are qualitatively identical, they are offset from one another due to the impact of low Reynolds numbers on thrust production discussed in 7.2.

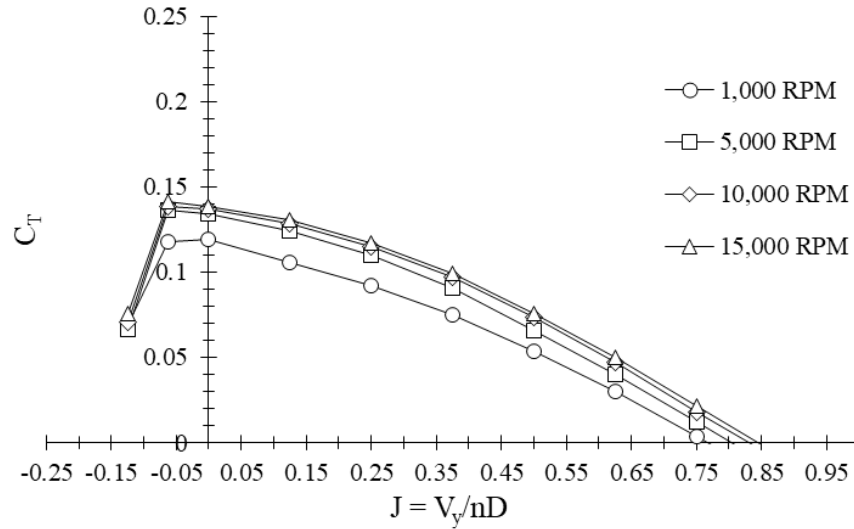


Figure 33: C_T vs J over a range of RPMs.

7.3.1 Ascending Flight

When the propeller is ascending, the aerodynamic angle of attack on the propeller blade is reduced, which in turn lowers the thrust produced by the propeller. This trend of reduction in thrust with increasing advance ratio is seen in previous experimental studies performed by Brandt (2005) and Deters et al. (2014) on propellers of similar sizes and Reynolds numbers. The reduction in aerodynamic angle of attack can be easily visualized using contours of RVM, seen below in Figure 34. The reduction in angle of attack is easily seen by the movement of the stagnation point from the bottom surface of the blade section in the static case to the very front of the blade section at $J = 0.75$. At these higher advance ratios, the velocity along the suction side of the blade section has become nearly equal to that of the pressure side, resulting in zero or negative thrust values at advance ratios higher than 0.75

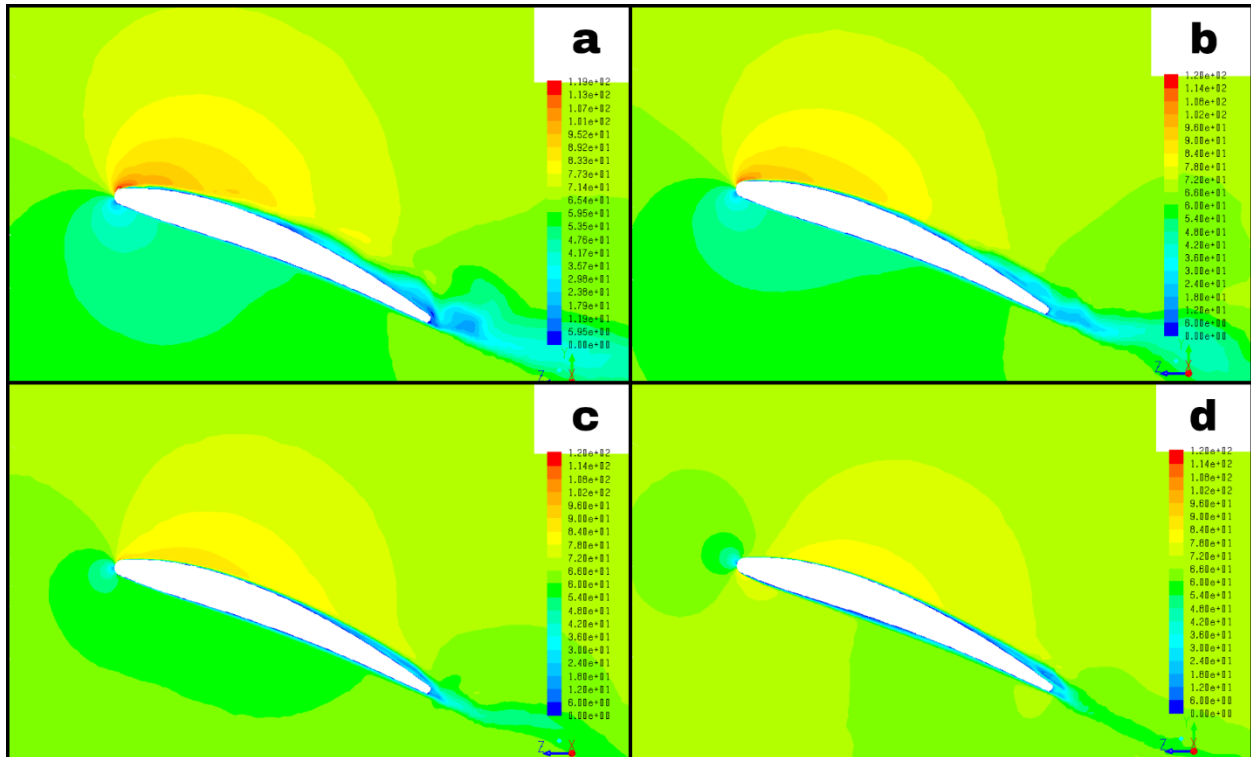


Figure 34: RVM contours at 10,000 RPM at span 0.7R a.) Static b.) $J = 0.25$ c.) $J = 0.50$ d.) $J = 0.75$

The reduction of thrust at higher advance ratios can also be explained by plots of C_P at different advance ratios in Figures 35 and 36. As advance ratio increases, the magnitude of the suction side C_P is reduced due to the reduction in velocity across the suction side of the blade section. Due to the movement of the stagnation from the bottom surface of the blade section to the leading edge, the C_P plots for the suction and pressure at $J = 0.75$ become distorted as the stagnation point crosses the parting line that separates the pressure and suction sides.

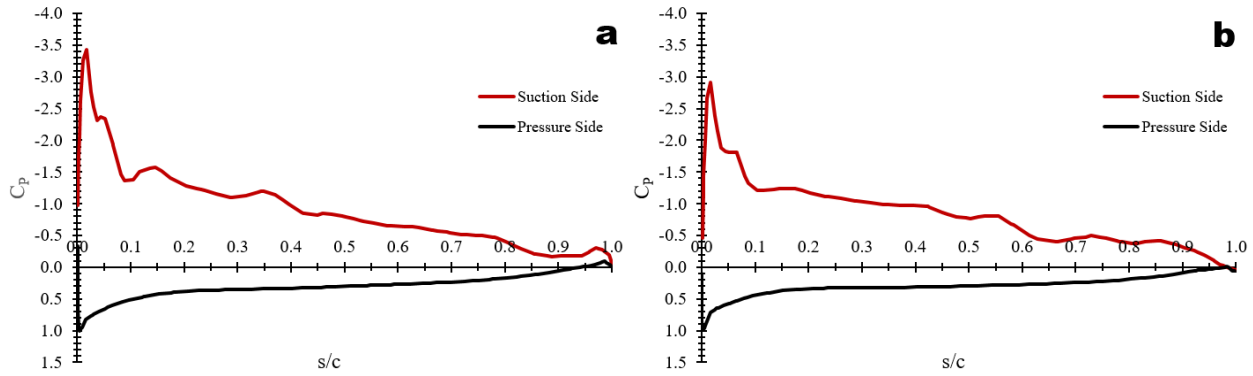


Figure 35: C_P vs s/c at span $0.7R$, a.) Static b.) $J = 0.25$

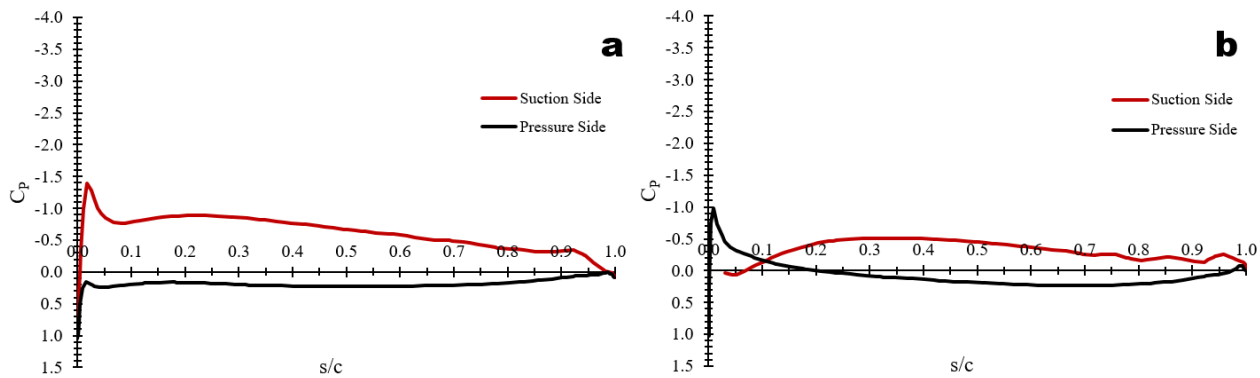


Figure 36: C_P vs s/c at span $0.7R$, a.) $J = 0.50$ b.) $J = 0.75$

Though no experimental data for C_T as a function of advance ratio was available for the DD7x4.5 propeller, the work of Kutty et al. (2017) suggests that FLUENT based CFD is able to accurately capture the trend of C_T/C_{T0} within five percent of experimental values below advance ratios of 0.7.

7.3.2 Descending Flight

When the propeller is descending, the aerodynamic angle of attack on the blades is increasing. As a result, C_T experiences an increase at small negative advance ratios before experiencing a drastic decrease, analogous to the maximum lift coefficient experienced by a fixed finite wing or airfoil before stalling. Contours of RVM in Figure 37b at $J = -0.125$ show the

beginnings of stall, with flow separation increasing along the suction side of the blade section. The separation bubble, which mostly reattaches and closes in the static case, remains open at $J = -0.125$ as the blade stalls. This behavior is also reflected in the plots of C_p in Figure 38.

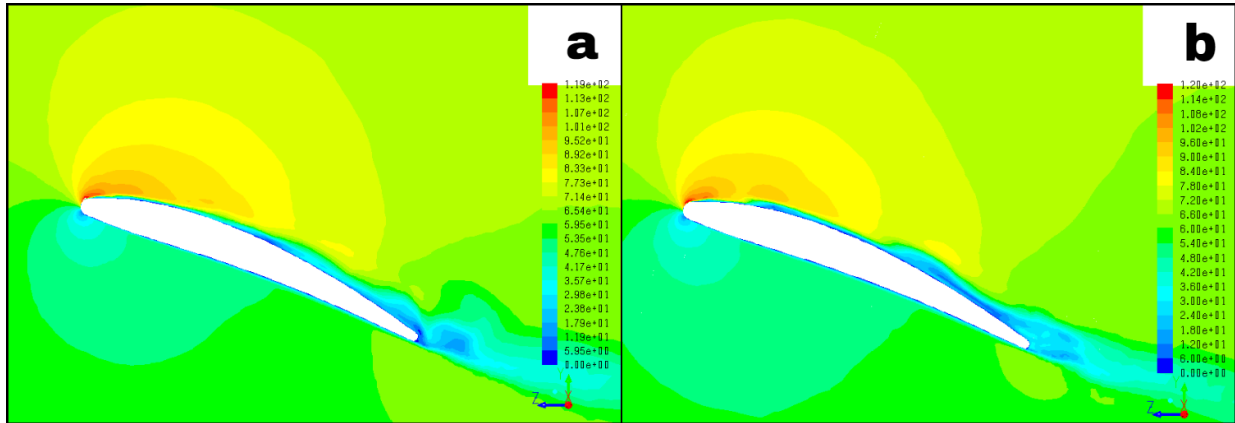


Figure 37: RVM Contours at 10,000 RPM, span 0.7R a.) Static b.) $J = -0.125$

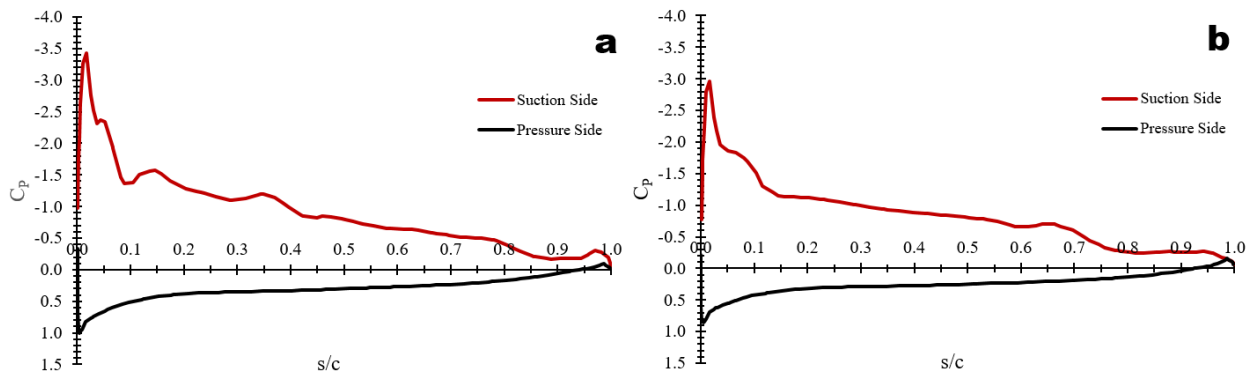


Figure 38: C_p vs s/c at 10,000 RPM, span 0.7R a.) Static b.) $J = -0.125$

The stalling of the propeller's blades at such small negative advance ratios can also be explained by the phenomenon known as 'vortex-ring state'. As with fixed wings, vortices at the tips of the blades are formed as the blades travel. When the propeller is descending, there is an increased upflow of air at the tips of the blades that increases the strength of the vortices. Because the vortex travels with the blades, this forms a vortex ring at the outer edge of the propeller disk.

This reduces the thrust generated, resulting in an increased flow of air at the blade roots. This can increase the local angle of attack at the root such that the blade stalls. To capture these vortices, surfaces of normalized Q-criterion are presented in Figures 36 and 37. Q-criterion as defined by Hunt et al. (1988) is calculated using the magnitudes of vorticity and strain rate:

$$Q_{crit} = \frac{1}{2}(\omega^2 - \dot{\epsilon}^2) \quad (26)$$

Because Q can span a wide range of values and make it difficult to isolate a vortex core within the flow field, the normalized Q-criterion is defined as:

$$Q_{norm} = \frac{(\omega^2 - \dot{\epsilon}^2)}{(\omega^2 + \dot{\epsilon}^2)} \quad (27)$$

This value always lies between -1 and 1, making isolating a vortex core a simpler task. Isosurfaces of normalized Q-criterion are presented below in Figures 39 and 40 for the static case and the descending advancing case.

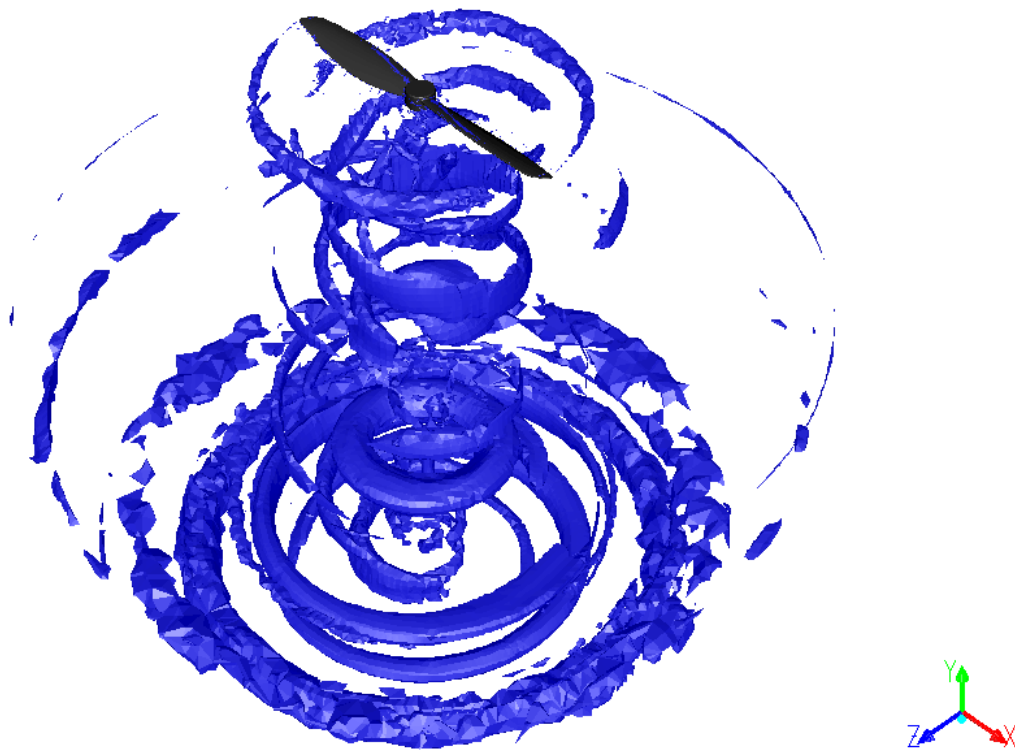


Figure 39: Isosurface of $Q_{norm} = 0.75$ at 10,000 RPM, static

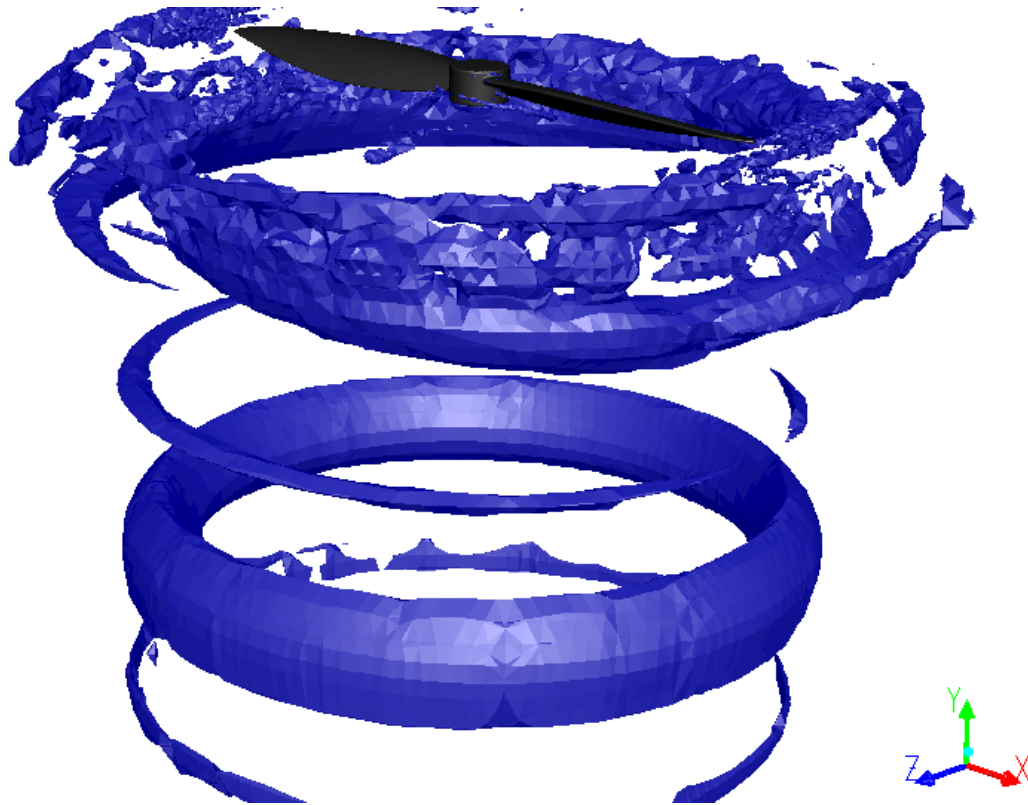


Figure 40: Isosurface of $Q_{\text{norm}} = 0.75$ at 10,000 RPM, $J = -0.125$.

In the static case, the vortices do not surround the edges of the blades in a manner that would lead to increased angle of attack on the blades. For $J = -0.125$, the vortex cores surround the blades in a manner that resembles a donut, leading to increased angle of attack across the blades, which then helps to stall the blades. The combination of the descent rate and the vortex rings lead to aerodynamic stall of the blades at a relatively small negative advance ratio, which in turn leads to a considerable reduction in thrust.

7.4 Ground Effect Cases

The effect of ground proximity on propeller thrust performance was small when compared to the effects from other variables. At 10,000 RPM and $h/D = 0.57$ ($h = 4\text{in}$), C_T increased by six

percent when compared to the C_{TOGE} (C_T out of ground effect) at the same RPM. This trend can be seen across all RPMs with the exception of the very low RPM range (1,000-2,000 RPM). The minimum h/D value tested in the simulations was $h/D = 0.57$, corresponding to the minimum ground proximity at which the UAV can expect to operate. Results from these simulations can be seen below in Figure 41. With the exception of 1,000 RPM and 2,000 RPM, C_T increases by six percent when compared to C_{TOGE} at $h/D = 0.57$. The C_T returns to values in line with those in the far field at $h/D = 1.43$ ($h = 10\text{in}$).

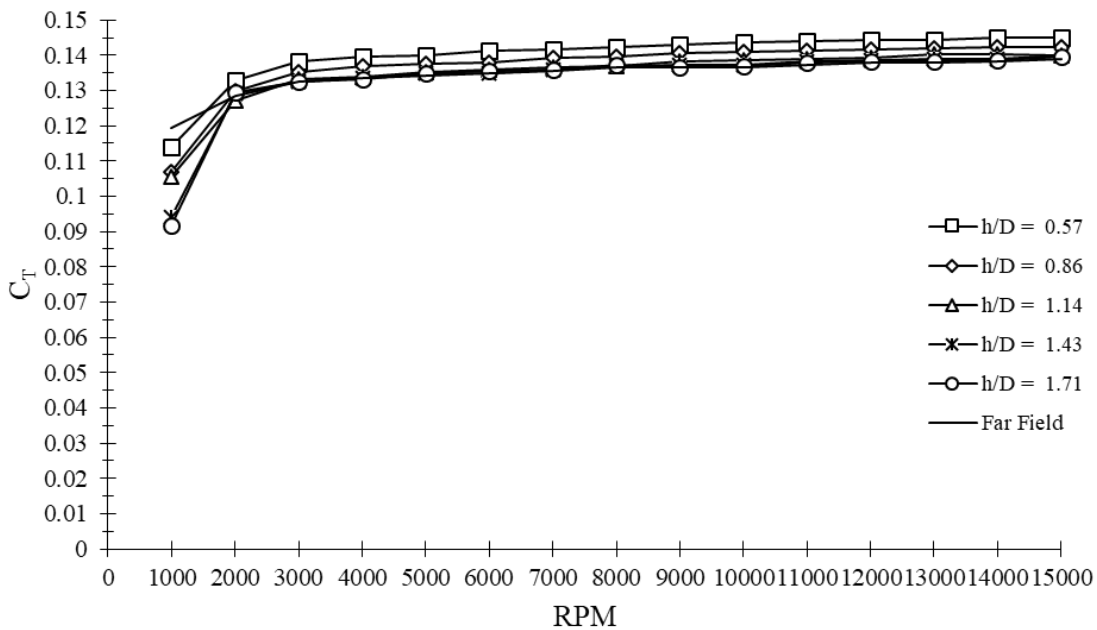


Figure 41: C_T vs RPM at a variety of h/D values

The results from CFD are quantitatively similar to those from the experimental measurements in 4.3 and also experimental measurements from previous studies. Figure 42 depicts the ratio of C_T to C_{TOGE} at 10,000 RPM over a range of h/D values for the DD7x4.5 (CFD and experimental) and the APC 11x5.5 at 6,000 RPM (Cai et al. 2019). The CFD results capture trends of C_T equally as effectively as the experimental measurements from 4.3, and compare well with the results from the APC 11x5.5 at 6,000 RPM.

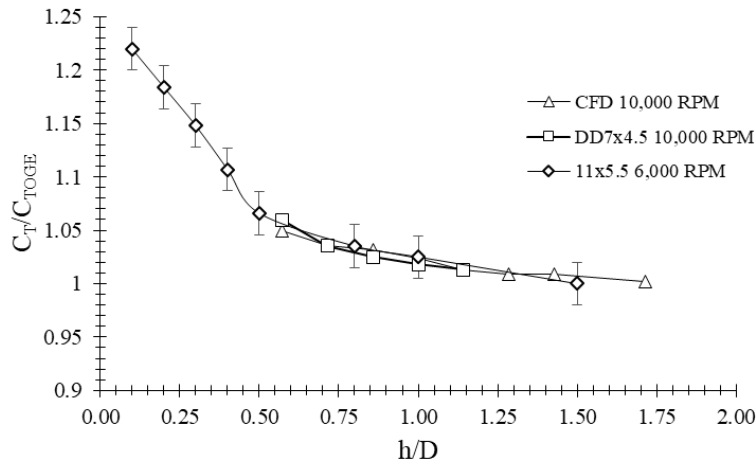


Figure 42: $C_T/C_{T_{TOGE}}$ vs h/D for the DD7x4.5 (CFD and Experimental) and 11x4.5

Though it proved difficult to study the qualitative impact of the ground on the downstream flow field within the simulations (as done experimentally in Lee et al., 2010), the impact of the ground on the propeller's aerodynamics can be visualized through its impact on pressure coefficient. Figures 43, 44, and 45 illustrate C_p as a function of s/c for various ground proximities at 10,000 RPM. The magnitude of the peak suction side C_p decreases as h/D increases, and eventually levels off at $h/D = 1.43$. Pressure side C_p is unaffected. The suction side C_p along the rest of the blade section also experiences minute increases.

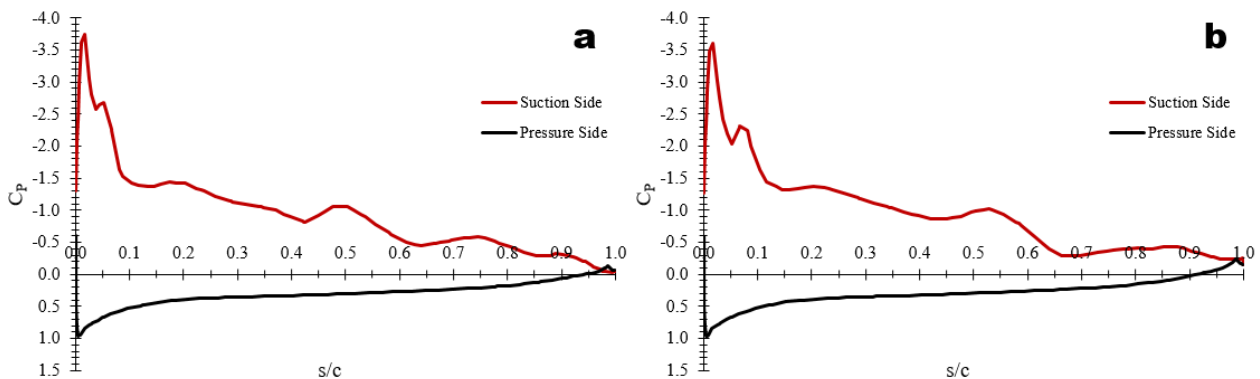


Figure 43: C_p vs s/c at span 0.7R, 10,000 RPM a.) $h/D = 0.57$ b.) $h/D = 0.71$

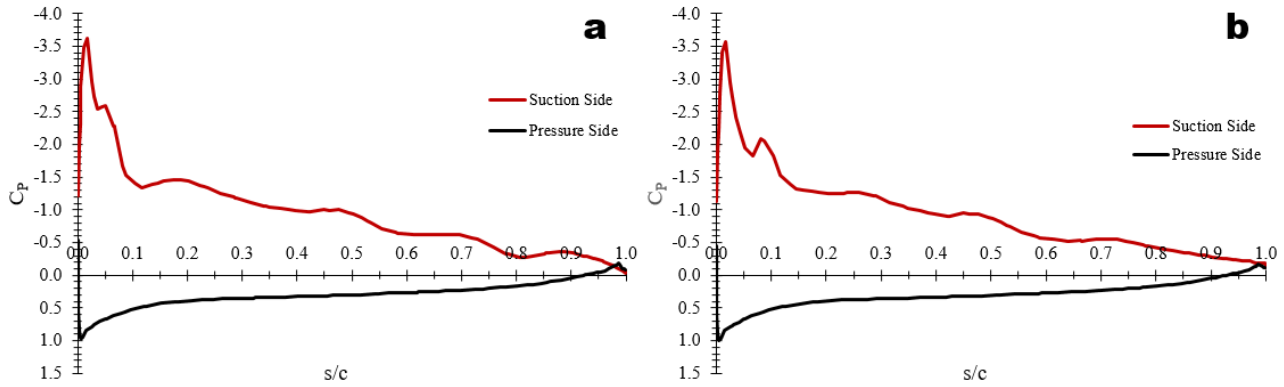


Figure 44: C_P vs s/c at span $0.7R$, $10,000$ RPM a.) $h/D = 0.86$ b.) $h/D = 1.00$

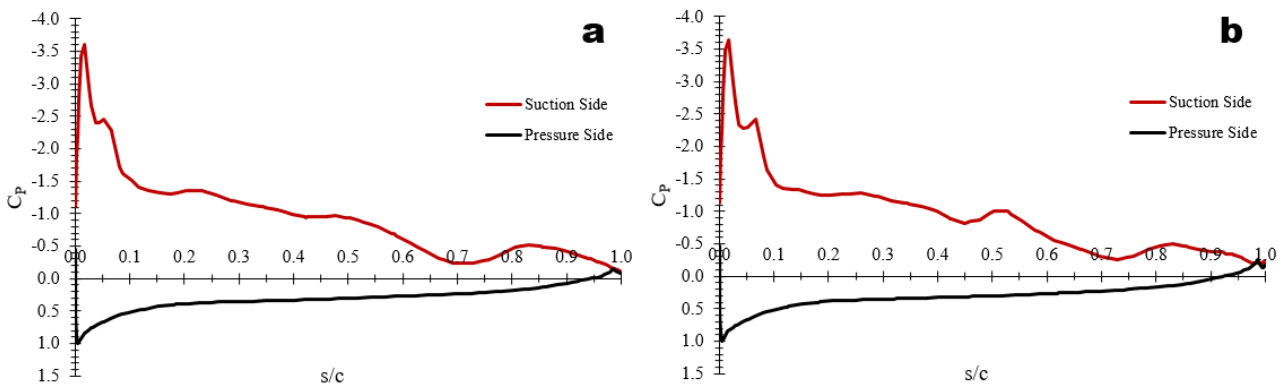


Figure 45: C_P vs s/c at span $0.7R$, $10,000$ RPM a.) $h/D = 1.14$ b.) $h/D = 1.43$

The changes in suction side C_P are more easily visualized in the following plot of suction side C_P vs s/c at a variety of h/D values in Figure 46. Though the change in C_P is less perceivable than seen with changes in Reynolds number and axial advance ratio, the small changes in suction side C_P are comparable in magnitude to the similarly small changes in thrust production shown in Figures 41 and 42.

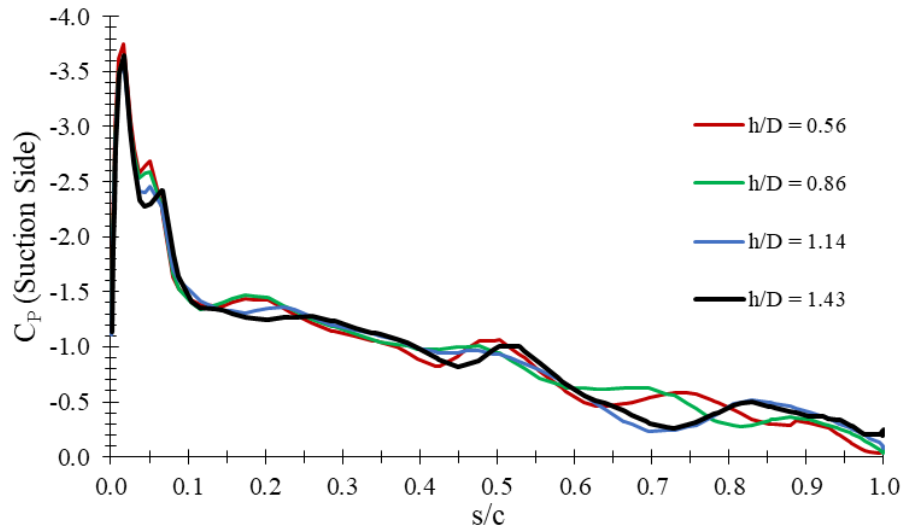


Figure 46: Suction Side C_p vs s/c at span $0.7R$, $10,000$ RPM, at a variety of h/D values

7.5 Crosswind Cases

The effect of crosswind flow across the propeller disk can be illustrated by plotting C_T as a function of the transverse advance ratio at several RPMs as computed by CFD. This plot is seen in Figure 47. The curves at different values of RPM are qualitatively alike, but exhibit the same offset seen in Figure 30 (C_T vs J) due to low Reynolds number effects at low values of RPM. The curves of C_T with respect to μ are proportional to V_z^2 , but are relatively shallow.

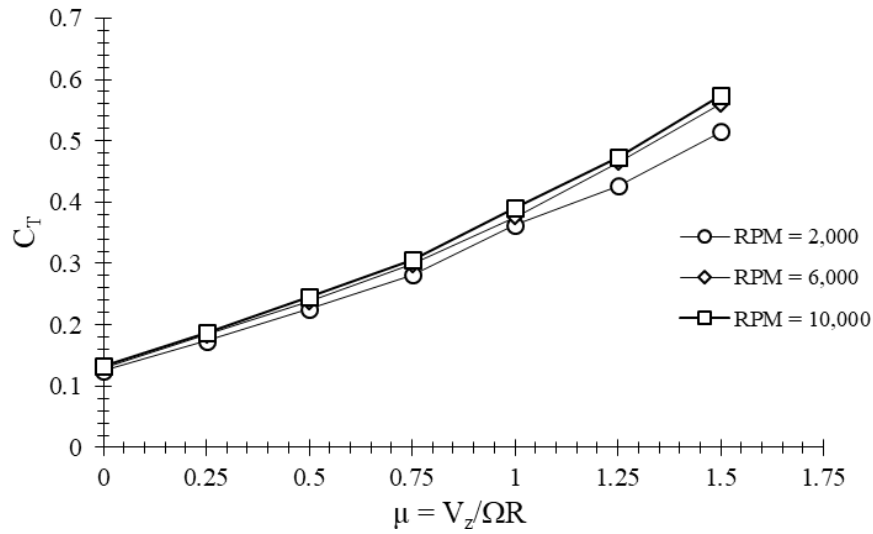


Figure 47: C_T vs μ at several RPMs

Due to CFD simulations studying crosswind effects being run as transient simulations, the impact of crosswinds on thrust production changes at each point in the propeller blade's rotation, as illustrated in Figure 22. For the purpose of studying crosswind effects as the blades rotate, the angle Φ is defined as the blade rotation angle. When Φ is 0° , the axis of the blades' span is orthogonal to the incoming crosswind. When Φ is 90° , the axis of the blades' span is parallel to the incoming crosswind, and the crosswind is running directly down the span of the blades.

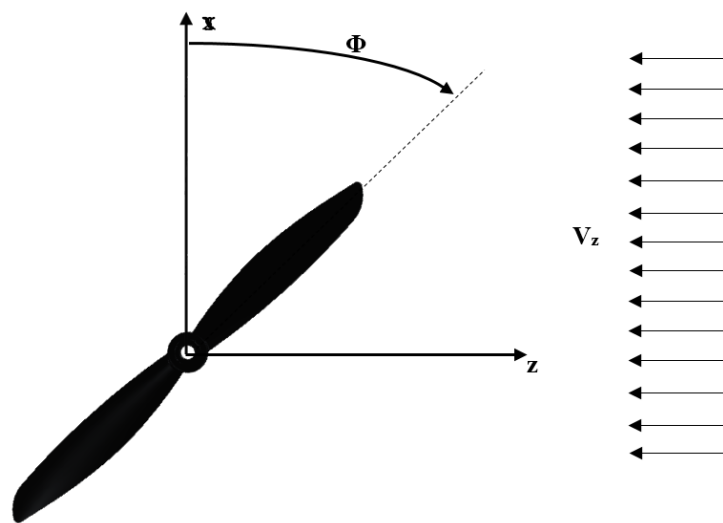


Figure 48: Blade rotation angle Φ shown in relation to crosswind velocity field V_z

To further illustrate the impact of crosswind on thrust production as the blades rotate, contours of static pressure on the blade surface are presented at different blade rotation angles. Since thrust is a product of pressure differences between the suction and pressure sides of the blades, more negative values of static pressure on the suction side and more positive values of static pressure on the pressure side indicate higher levels of thrust.

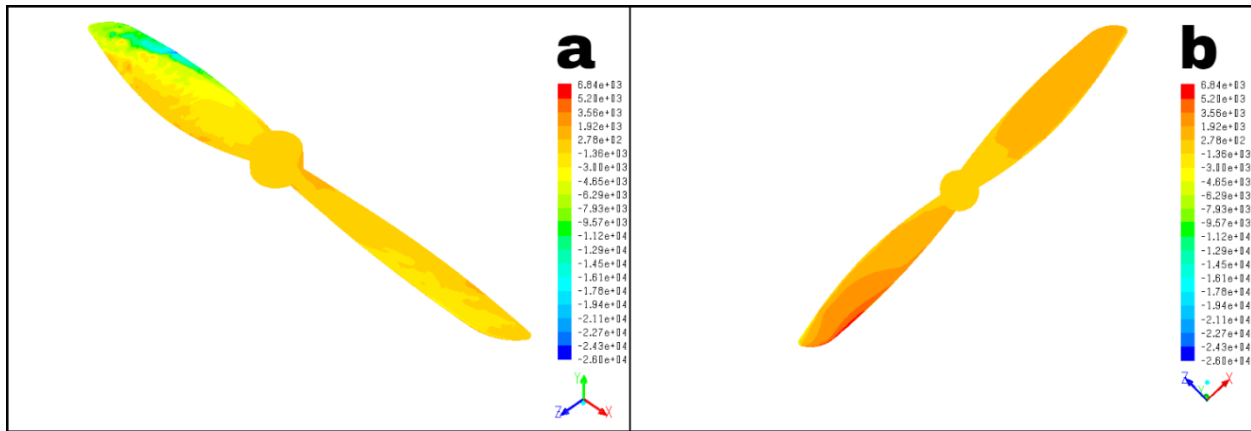


Figure 49: Contours of static pressure on the propeller blades' surface at 10,000 RPM, $\mu = 0.25$, $\Phi = 0^\circ$ a.) suction side b.) pressure side

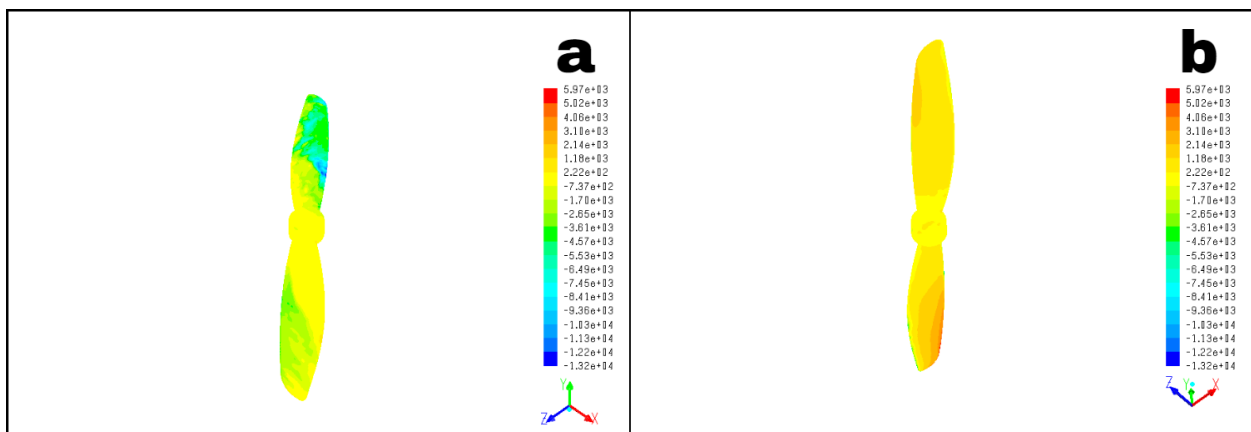


Figure 50: Contours of static pressure on the propeller blades' surface at 10,000 RPM, $\mu = 0.25$, $\Phi = 45^\circ$ a.) suction side b.) pressure side

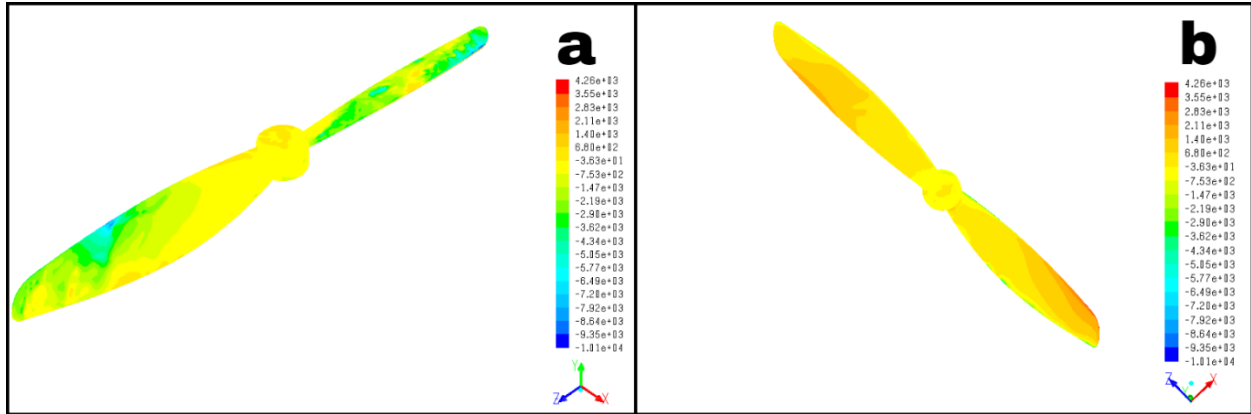


Figure 51: Contours of static pressure on the propeller blades' surface at 10,000 RPM, $\mu = 0.25$, $\Phi = 90^\circ$ a.) suction side b.) pressure side

The asymmetry in static pressure seen at $\Phi = 0^\circ$ is due to the advancing blade (leftmost in the figures) experiencing higher relative velocities than the retreating blade (rightmost in the figures).

At this point in the blade's rotation, the thrust produced is at a maximum, as illustrated below in Figure 52.

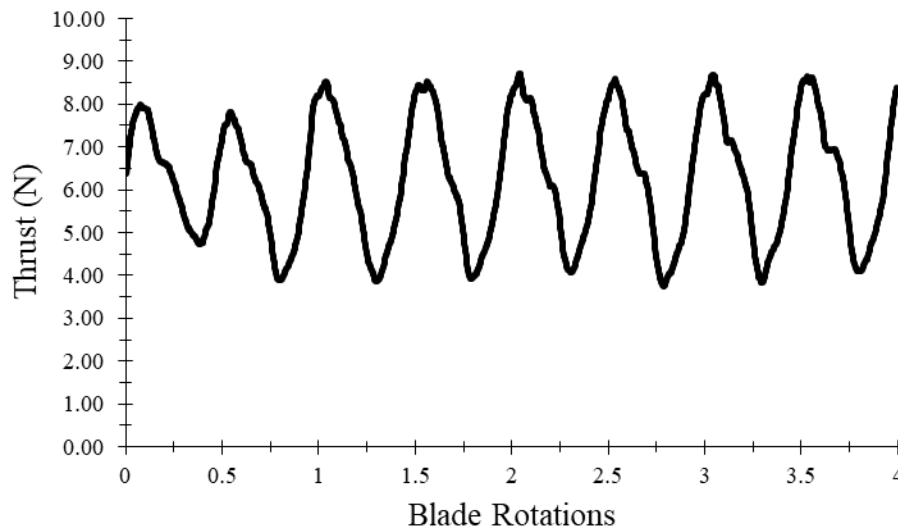


Figure 52: Propeller thrust as the blades rotate at 10,000 RPM, $\mu = 0.25$

At $\Phi = 45^\circ$, the asymmetry in static pressure (and by extension, thrust) between the advancing blade (topmost in Figure 49a, bottommost in Figure 49b) and retreating blade (bottommost in

Figure 49a, topmost in Figure 49b) has lessened, but is still easily visible. At $\Phi = 90^\circ$, this asymmetry has become negligible, as both blades experience nearly identical pressure distributions on both the pressure and suction sides. At this point in the blade's rotation, thrust is at its minimum. Though the increases in thrust are proportional to V_z^2 , the rotation of the blades ensures that magnitude of these increases change as the blades rotate.

As transverse advance ratio increases, velocity across the advancing blade increases, which increases the thrust produced on the advancing blade. The opposite is true on the retreating blade, as thrust is reduced due to the relative velocity across it decreasing. The asymmetry in thrust production becomes more pronounced as transverse advance ratio increases and is reflected in plots of static pressure on the blade surface in Figures 53, 54, 55, and 56. At $\mu = 0.00$ (static case), the pressure distribution (and by extension, the thrust distribution) is identical on both blades. At $\mu = 0.25$, the static pressure advancing blade (leftmost in the figures) is noticeably more negative on the suction side and higher on the pressure side than on the retreating blade (rightmost in the figures), where the difference in pressures between the suction and pressure sides of the blade is shrinking. These observations are more pronounced at $\mu = 0.75$, where the flow for 75 percent of the retreating blade's span has reversed due to the crosswind component of the relative velocity becoming greater than the velocity component due to the local rotational speed. At $\mu = 1.25$, the asymmetry in static pressure distribution between the advancing and retreating blades has become extremely pronounced. Due to the entire retreating blade experiencing reversed flow at this stage, air is redirected upwards, producing negative thrust. This is evidenced by the static pressure on the pressure side becoming negative, and the static pressure on the suction side becoming positive. The retreating blade generates this negative thrust much less efficiently than the advancing blade generates positive thrust at this condition, as the retreating blade's airfoil sections are, in effect,

flying backwards, or trailing edge first. As μ increases, this will result in larger and larger asymmetries in thrust production between the advancing and retreating blades. Consequently, the thrust production increases with V_z^2 , despite the retreating side becoming less and less effective at generating positive thrust.

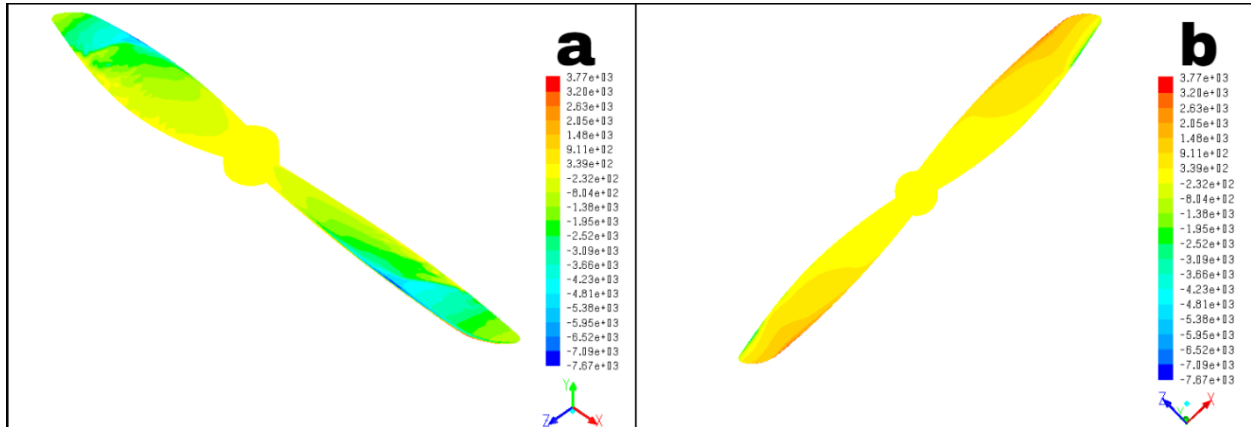


Figure 53: Contours of static pressure on the propeller blades' surface at 10,000 RPM, $\mu = 0.00$, $\Phi = 0^\circ$ a.) suction side b.) pressure side

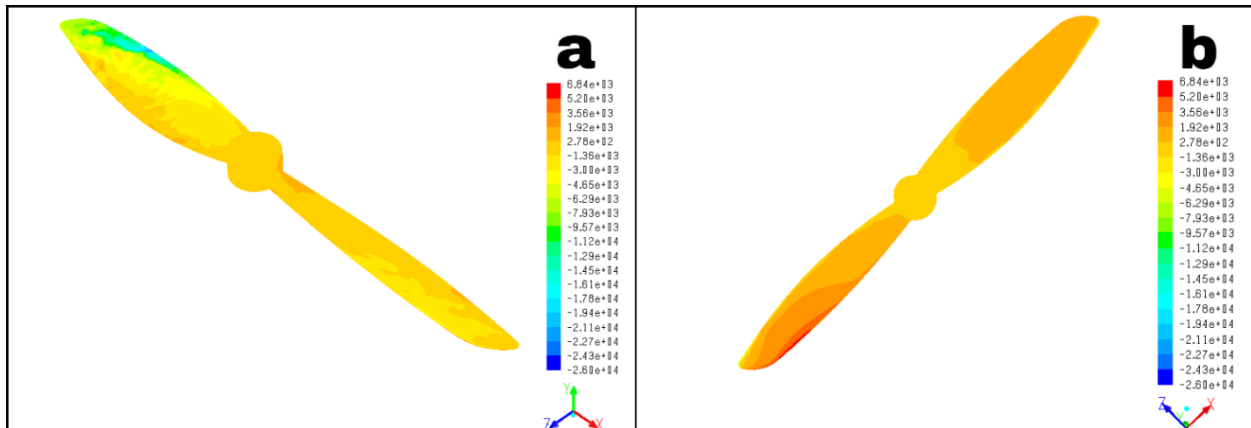


Figure 54: Contours of static pressure on the propeller blades' surface at 10,000 RPM, $\mu = 0.25$, $\Phi = 0^\circ$ a.) suction side b.) pressure side

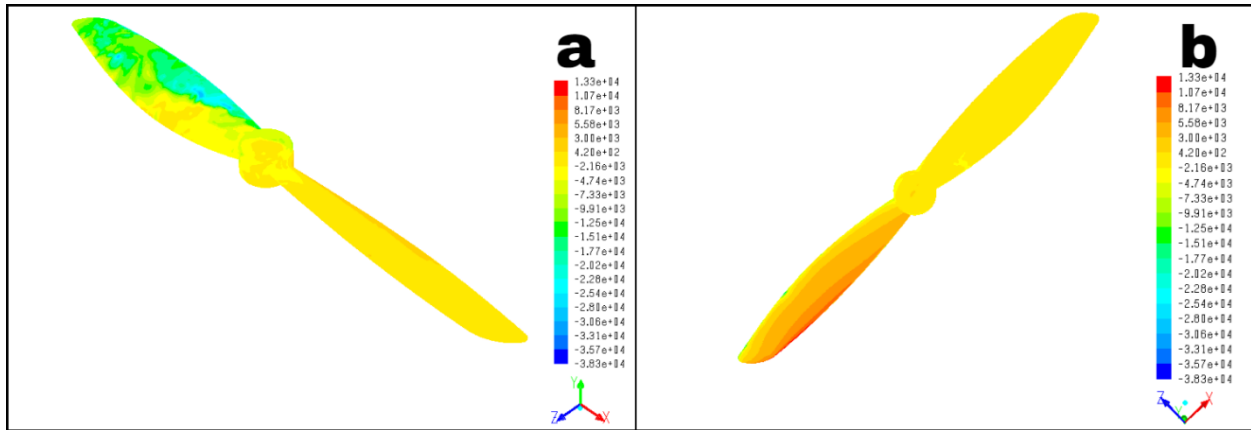


Figure 55: Contours of static pressure on the propeller blades' surface at 10,000 RPM, $\mu = 0.75$, $\Phi = 0^\circ$ a.) suction side b.) pressure side

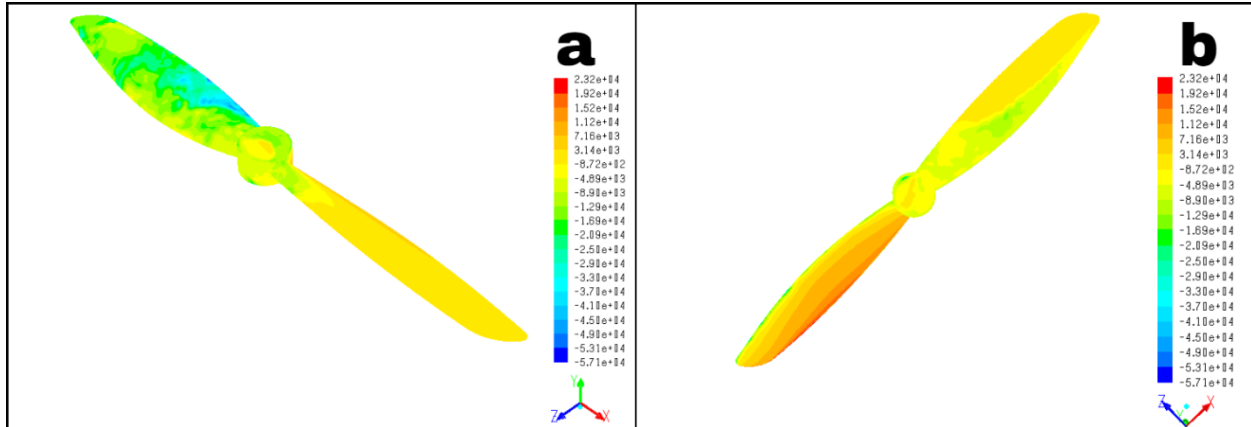


Figure 56: Contours of static pressure on the propeller blades' surface at 10,000 RPM, $\mu = 1.25$, $\Phi = 0^\circ$ a.) suction side b.) pressure side

7.6 Final Empirical Thrust Model

The data from the experimental measurements and CFD simulations were used to create an empirical thrust model. Since thrust production as a function of advance ratio, ground proximity, and crosswind remained qualitatively unchanged with RPM, the following model was used:

$$C_T = C_{T0} \times RC_{T,J} \times RC_{T,h} \times RC_{T,\mu} \quad (28)$$

In this multiplicative model, C_{T0} is the static, far-field thrust coefficient as a function of RPM. The multiplier $RC_{T, J}$ represents C_T/C_{T0} as a function of axial advance ratio, $RC_{T, h}$ represents C_T/C_{TOGE} as a function of h/D , and $RC_{T, \mu}$ represents C_T/C_{T0} as a function of transverse advance ratio. The model assumes effects from J , h/D , and μ to be multiplicative even when values of all three parameters are not equal to one. Additional verification of this assumption is presented in section 7.6.5. The curves used to model the trends captured in these multipliers were created in MATLAB's curve-fitting toolbox.

7.6.1 RPM Dependence

Before fitting a curve to the C_{T0} vs RPM curve, the data points were anchored using the data from the experimental measurements in 4.3. The CFD data was biased to a 20 percent over-prediction when compared to the experimental data. To anchor these points, each value of C_{T0} was multiplied by 0.83 to achieve the 'true' curve of static thrust. The curve fit to the resulting anchored data was a rational function of the following form:

$$C_{T0} = \frac{p_1RPM^4 + p_2RPM^3 + p_3RPM^2 + p_4RPM + p_5}{RPM^3 + q_1RPM^2 + q_2RPM + q_3} \quad (29)$$

The resulting curve had an R^2 value of 0.9945 and a sum-of-squares due to error value (SSE) of 1.13×10^{-6} .

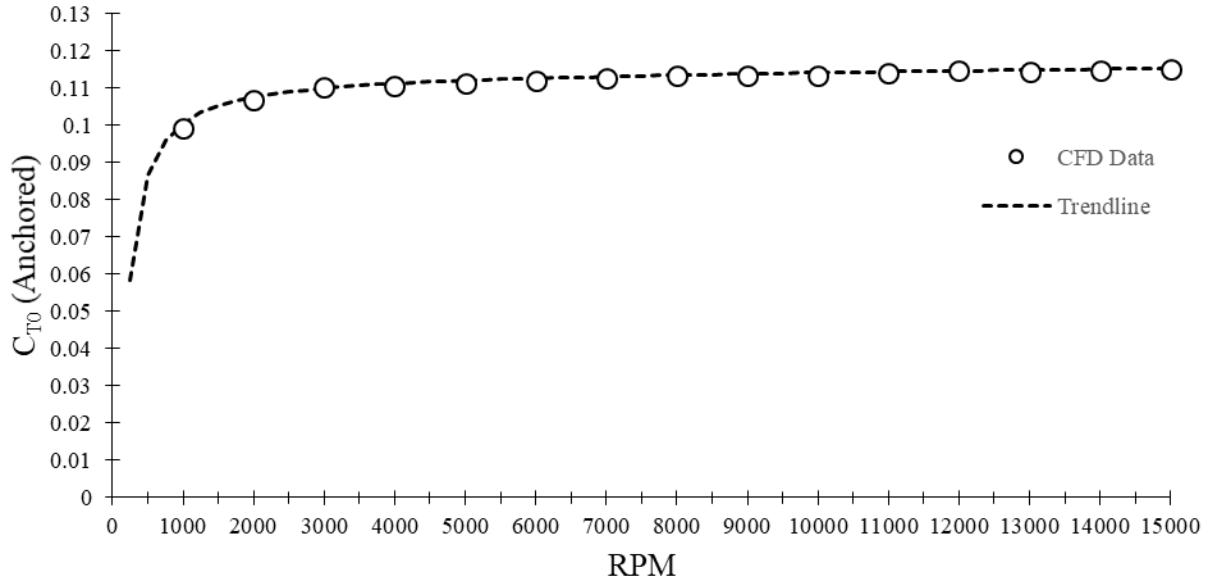


Figure 57: Anchored C_{T0} values vs RPM, with trendline shown.

7.6.2 Advance Ratio Dependence

The change in thrust coefficient as a function of advance ratio was curve fitted using a rational function of the following form:

$$RC_{TJ} = \frac{p_1 J^2 + p_2 J + p_3}{J^2 + q_1 J + q_2} \quad (30)$$

The resulting curve had an R^2 value of 0.9938 and an SSE value of 0.0073. Due to the propeller experiencing an abrupt reduction in thrust production at small negative advance ratios, there exists a small discrepancy between the fitted curve and the data points in this flow regime.

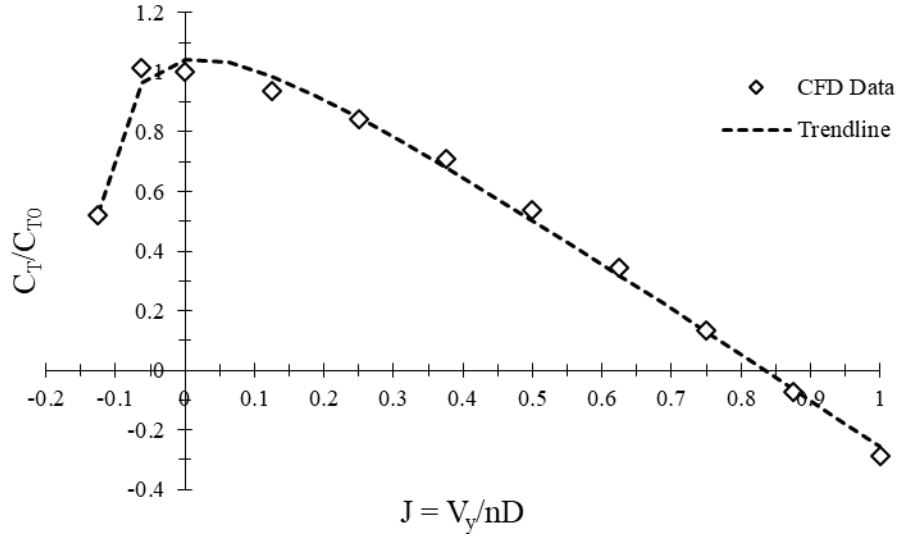


Figure 58: C_T/C_{T0} vs advance ratio values with trendline shown.

7.6.3 Ground Effect Dependence

The curve fit for the change in thrust coefficient as a function of h/D was a four term Gaussian function of the following form:

$$RC_{T,h} = a_1 e^{-\left[\frac{(h/d)-b_1}{c_1}\right]^2} + a_2 e^{-\left[\frac{(h/d)-b_2}{c_2}\right]^2} + a_3 e^{-\left[\frac{(h/d)-b_3}{c_3}\right]^2} + a_4 e^{-\left[\frac{(h/d)-b_4}{c_4}\right]^2} \quad (31)$$

The resulting curve had an R^2 value of 0.9701 and an SSE value of 2.46×10^{-6} .

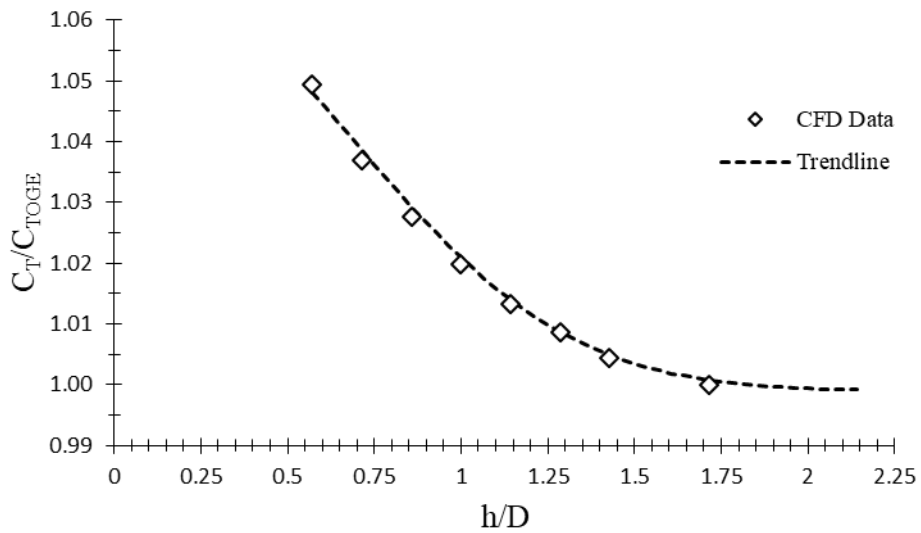


Figure 59: C_T vs C_{TOGE} vs h/D with trendline shown.

7.6.4 Crosswind Dependence

The curve fit for the change in thrust coefficient as a function of transverse advance ratio was a second order polynomial of the following form:

$$RC_{T,\mu} = p_1\mu^2 + p_2\mu + p_3 \quad (32)$$

The resulting curve had an R^2 value of 0.9991 and an SSE value of 0.0069.

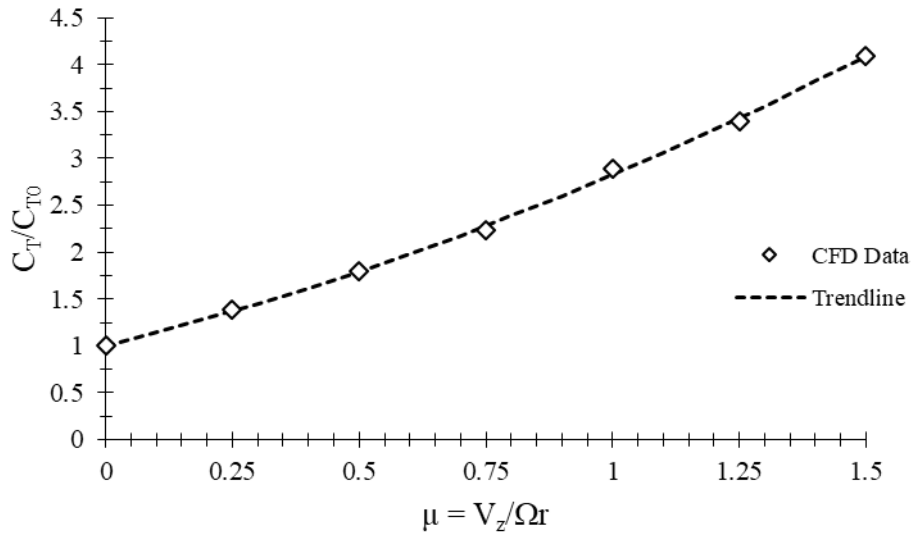


Figure 60: C_T/C_{T0} vs transverse advance ratio values with trendline shown.

7.6.5 Complete Model

The completed empirical model was tested against both computed values from the CFD simulations and also against computed values from the older thrust model it is meant to replace. The older model represents thrust as purely a static, far-field case, with no variance in thrust due to axial advance ratio, crosswinds, or ground proximity.

$$T_{old} = K \times RPM^2 \quad (33)$$

This model assumes C_T to purely be a function of the propeller's design, and it is incorporated into the K term along with the ambient air density and propeller diameter.

The final empirical thrust model was tested against anchored thrust predictions from the CFD simulations. The results from these tests are presented below in Table 8.

Table 8: Thrust predictions from empirical model vs that of CFD simulations

Case Description	Thrust (N), New Model	Anchored Predicted Thrust (N), CFD	Error Magnitude (%)
Static, 1,000 RPM	0.034	0.031	4.28
Static, 10,000 RPM	3.74	3.58	4.54
J = 0.5, 12,000 RPM	2.61	2.71	3.69
J = -0.0625, 15,000 RPM	7.87	8.32	5.36
$\mu = 0.25$, 10,000 RPM	5.11	5.06	0.93
$\mu = 1.25$, 10,000 RPM	12.79	12.77	0.13
h/D = 0.56, 8,000 RPM	2.49	2.38	4.42
$\mu = 0.25$, J = 0.375, 10,000 RPM	3.33	3.23	6.32

Error magnitudes resulting from imperfect curve fitting were kept to a minimum, generally below five percent. The largest error magnitudes were predictions involving negative advance ratios and cases where a combination of the tested variables was employed. The curve fit for C_T/C_{T0} vs axial advance ratio had its largest discrepancy at small negative advance ratios, due to the non-smooth nature of the data points. The last case listed in the above table is a case where the propeller experiences a combination of incoming axial flow and incoming crosswind. This case was run in order to test the empirical model's multiplicity, as it was not practical to simulate every combination of every variable. The level of error for this multiplicative case, and that of the other listed cases, was deemed acceptable, as these levels of error represented an immense improvement over the previously used model described by equation 33. The discrepancies in thrust predictions between the new and old models are given below in Table 9.

Table 9: Percent difference in thrust predictions from new model and old model

Case Description	Thrust (N), New Model	Thrust (N), Old Model	Variation Between Old and New Models (%)
J = 0.25, 10,000 RPM	3.04	3.92	28.84
J = 0.75, 10,000 RPM	0.46	3.92	746.09
J = -0.125, 5,000 RPM	0.46	0.97	108.89
h/D = 0.6, 15,000 RPM	8.91	8.85	0.67
h/D = 0.5, 10,000 RPM	3.94	3.91	0.79
$\mu = 0.25$, 10,000 RPM	5.11	3.92	23.37
$\mu = 0.75$, 10,000 RPM	8.51	3.92	53.97
$\mu = 1.25$, 10,000 RPM	12.79	3.92	69.39

With the exception of cases involving ground effect, the discrepancies between the old, static model and the empirical model from CFD are large. At larger axial advance ratios, these discrepancies are on the order of hundreds of percentage points. Discrepancies at other operating conditions are on the order of 50-100 percent. Though the empirical model has small amounts of error compared to CFD predictions due to imperfect curve fitting, it still represents a substantial improvement in predictive capability across most of the operating regime when compared to the previously used model described by equation 33.

The improved thrust prediction capabilities provided by the new empirical thrust model will allow the UAV reach its desired state (e.g. velocity and position) significantly faster than was possible using the older thrust model used in most quadrotor control systems. The UAV's control system will use the model to predict the required RPM from its propellers to achieve a required amount of thrust for a given set of operating conditions and control commands. The required RPM can be expressed by rearranging the equation for propeller thrust:

$$RPM = 60 \sqrt{\frac{T_{req}}{\rho D^4 C_T}} \quad (34)$$

In this model with RPM as the desired quantity, T_{req} is the required thrust as computed by the UAV's control system, ρ is the ambient air density, D is the propeller diameter, and the thrust

coefficient C_T is computed using a modified version of the empirical model expressed in equation 28. Since required RPM is the desired quantity, C_T must not depend on RPM in order to avoid a circular reference. To avoid this, C_{T0} in equation 29 is assumed to be 0.113, which will hold true for all but the lowest RPM range. For this formulation, C_T is only a function of J , h/D , and μ . The model for required RPM is now purely a function of the required thrust, with C_T continuously calculated based on the operating conditions of the UAV.

Chapter VIII

Conclusions and Future Work

8.1 Conclusions

CFD simulations of the DD7x4.5 propeller were performed from 1,000 RPM to 15,000 RPM over ranges of axial advance ratios, ground proximities, and transverse advance ratios. The simulations were carried out using an assumption of laminar flow, although preliminary verification simulations showed similar results obtained when using RANS-based CFD with common eddy-viscosity turbulence models. The results for the static and ground effect cases were compared to experimental data obtained from testing the actual DD7x4.5 propeller with a commercial thrust measurement stand. The CFD and experimental results were compared in terms of thrust coefficient. The CFD simulations were used to explain differences in thrust between different operating conditions via plots of C_P , RVM, C_f , τ_w , and p_{static} . The experimental data was used both for validation of trends and to anchor the thrust values captured by the CFD simulations under different operating conditions. Numerical curve fitting was then employed to create an empirical thrust model from the anchored data.

The experimental studies highlighted small, steady increases in C_{T0} with increasing Reynolds number and mild increases in C_T with decreased ground proximity. The C_T data was considered to be unreliable at low RPMs due to the resolution of the instrument used and this data was not included. Despite this, the linear region of the experimental C_{T0} curve provided an anchor point for the CFD data, and the C_T data from the ground effect experiments provided validation for the later CFD simulations.

Several test cases were performed for the CFD simulations. The impact of using different boundary conditions was tested, and the choice of boundary condition was found not to impact the

thrust predictions. Crosswind cases required the use of transient simulations instead of steady state simulations, so it was necessary to test whether the addition of the unsteady term would impact the reported thrust. A 2.5 percent discrepancy was found between the steady state and transient simulations due to differences in instantaneous and time-averaged boundary layer behavior. This difference was deemed to be inconsequential due to its small magnitude and the fact that the CFD simulations would be used to capture trends, and any such discrepancies would be absorbed when the data was anchored by the experimental data. The final test cases were those using turbulence models and those not using turbulence models. Cases that did not use a turbulence model captured C_T trends equally as effectively as cases that employed the $k-k_l-\omega$ model and SST $k-\omega$ model, while the standard $k-\epsilon$ had significant convergence issues. As a result, all subsequent simulations were run without a turbulence model. Because the grid was refined enough to resolve small amounts of turbulence, the simulations were considered to be comparable to implicit large-eddy-simulations.

The CFD simulations of static propeller performance yielded C_T data that was consistently approximately 20 percent higher than the experimental data at RPM above 8,000. At lower RPMs, C_T degraded due to effects from low Reynolds numbers. These low Reynolds number effects were illustrated by plots of RVM and C_f , which showed considerable changes within the boundary layer with changing Reynolds number. These effects could be seen in all of the ensuing C_T curves. Simulations of the effect of axial advance ratio showed considerable degradation in thrust with increased J , with the propeller entering its windmilling state ($C_T < 0$) at $J > 0.75$. For descending flight, C_T increased at small negative values of J as the angle of attack increased to its critical point, then decreased as the blades stalled and experienced effects from vortex rings. These effects were elucidated by contours of RVM, plots of C_P along the chord of the blade, and isosurface plots of q -criterion to find vortex cores. Simulations to investigate the effect of ground proximity found

small, yet non-negligible effects on C_T at very small h/D values. These trends compared favorably qualitatively with experimental measurements. Simulations investigating the effect of crosswinds found that increased transverse advance ratios resulted in C_T values increasing by up to 400 percent and high thrust asymmetry between the advancing and retreating blades. Contours of static pressure illustrated that the advancing side is changed in a much more rapid manner, due to lift being proportional to V_z^2 .

Numerical curve fitting was used to create a multiplicative thrust model. The model uses the anchored static C_T data and multiplies it by a series of coefficients whose values are determined by C_T curves as a function of J , h/D , and μ . The curves fitted were rational functions for C_{T0} and J , a Gaussian curve for h/D , and a second-order polynomial for μ . The resulting model will replace an older model calculated thrust as purely proportional to $K \times \text{RPM}^2$. In addition to producing thrust predictions consistently within five percent of experimental and CFD data, the newer model was found to be vastly superior in predicting thrust in operating conditions that contain axial or transverse advance ratios. This newer model will allow for faster and more accurate responses for autonomous shipborne UAVs.

8.2 Future Work

Future efforts will fall into two categories: investigation into grid sizes and turbulence models, and cases involving larger propeller geometries and higher rotational speeds. Investigation into grid sizes and turbulence modeling could attempt to resolve the discrepancy between experimental and numerical thrust data via the use of successively finer grids, or coarser grids with different turbulence models. The potential also exists to use hybrid models combining LES and RANS. Future cases that investigate larger geometries and higher rotational speeds will lie in the

fully turbulent and possibly highly-compressible flow regimes. The impacts of density-based solvers and turbulence modeling will need to be investigated for these cases.

References

1. Alfonsi, G., "Reynolds-Averaged Navier–Stokes Equations for Turbulence Modeling," *Applied Mechanics Reviews*, vol. 62, Apr. 2009.
2. Barakos, G., and Garcia, A. J., "CFD analysis of hover performance of rotors at full- and model-scale conditions," *The Aeronautical Journal*, vol. 120, 2016, pp. 1386–1424.
3. Barth, T.J. and Jespersen, D.C., "The Design and Application of Upwind Schemes in Unstructured Meshes," *AIAA Journal* 89-0366 (1989).
4. Basaran, E. and Kaynak, U., "Propeller Performance Analysis Using Analytical and Numerical Methods," *ISER 93rd International Conference*, Dec. 2017.
5. Brandt, J. B., "Small-Scale Propeller Performance at Low Speeds," M.S. Thesis, Department of Aerospace Engineering, University of Illinois at Urbana-Champaign, Illinois, 2005.
6. Brandt, J., and Selig, M., "Propeller Performance Data at Low Reynolds Numbers," *49th AIAA Aerospace Sciences Meeting including the New Horizons Forum and Aerospace Exposition*, Apr. 2011.
7. Cai, J., Gunasekaran, S., Ahmed, A., and Ol, M. V., "Changes In Propeller Performance Due to Ground Proximity," *AIAA Scitech 2019 Forum*, Jun. 2019.
8. Deters, R. "Performance and Slipstream Characteristics of Small-Scale Propellers at Low Reynolds Numbers". Ph.D. Dissertation University of Illinois at Urbana-Champaign, 2014.

9. Deters, R. W., Krishnan, G. K. A., and Selig, M. S., "Reynolds Number Effects on the Performance of Small-Scale Propellers," 32nd AIAA Applied Aerodynamics Conference, 2014.
10. *FLUENT 16.2 Users Guide*, Lebanon, NH: Fluent Inc., 2015.
11. Hunt, J. C. R., Wray, A. & Moin, P., "Eddies, Stream, And Convergence Zones In Turbulent Flows," *Center for Turbulence Research Report*, 1988.
12. Jones, W., & Launder, B., "The Prediction of Laminarization With a Two-Equation Model of Turbulence," *International Journal of Heat and Mass Transfer*, 15(2), 301-314, 1972. doi:10.1016/0017-9310(72)90076-2.
13. Kamal, I. M. and Yusof, T. M., "A CFD RANS Cavitation Prediction For Propellers," *ARPJ Journal of Engineering and Applied Sciences*, vol 12, no 4, 2017, p. 1248.
14. Knight, M., and Hefner, R. A., "Analysis of Ground Effect on the Lifting Airscrew," *National Advisory Committee for Aeronautics*, Dec. 1941.
15. Kutty, H. A., and Rajendran, P., "Review on Numerical and Experimental Research on Conventional and Unconventional Propeller Blade Design," *International Review of Aerospace Engineering (IREASE)*, vol. 10, 2017, p. 61.
16. Kutty, H., and Rajendran, P., "3D CFD Simulation and Experimental Validation of Small APC Slow Flyer Propeller Blade," *Aerospace*, vol. 4, 2017, p. 10.
17. Lakshminarayan, V. K., Kalra, T. S., and Baeder, J. D., "Detailed Computational Investigation of a Hovering Microscale Rotor in Ground Effect," *AIAA Journal*, vol. 51, 2013, pp. 893–909.

18. Lee, T. E., Leishman, J. G., and Ramasamy, M., "Fluid Dynamics of Interacting Blade Tip Vortices with a Ground Plane," *Journal of the American Helicopter Society*, vol. 55, Jan. 2010, pp. 22005–2200516.
19. Liu, J., and Luo, S., "Navier-Stokes Equations based Flow Simulations of Low Reynolds Number Propeller for Unmanned Aerial Vehicle," *55th AIAA Aerospace Sciences Meeting*, May 2017.
20. Menter, F. R., "Two-Equation Eddy-Viscosity Turbulence Models for Engineering Applications," *AIAA Journal*, 32(8), 1598-1605, 1994.
doi:10.2514/3.12149.
21. Mohd, N. and Ridhwan, N. A., "Performance and Wake Analysis of Rotors in Axial Flight Using Computational Fluid Dynamics," *Journal of Aerospace Technology and Management*, vol 9, p. 192, 2017.
22. Mullenix, K. Q., "Investigation of Turbulence Model Performance In Computational Fluid Dynamics Simulations Of Horizontal Axis Wind Turbines," M.S. Thesis, Department of Aerospace and Mechanical Engineering, University of Oklahoma, 2019.
23. "Norman Mesonet," Mesonet Available: <https://www.mesonet.org/index.php>.
24. Patankar and Spalding, "A Calculation Procedure for Heat, Mass and Momentum Transfer in Three-dimensional Parabolic Flows." *International Journal of Heat and Mass Transfer* 15.10, 1787-806, 1972.
25. Patel, Y., "CFD Analysis of Propeller Blade Design for Quadrotor." M.S. Thesis, Delhi Technological University, 2016.

26. *Performance of Propellers*. Available:
<https://web.mit.edu/16.unified/www/FALL/thermodynamics/notes/node86.html>.
27. Qu, Q., Lu, Z., Liu, P., and Agarwal, R. K., "Numerical Study of Aerodynamics of a Wing-in-Ground-Effect Craft," *Journal of Aircraft*, vol. 51, 2014, pp. 913–924.
28. Ramakrishna, S., Ramakrishna, V., Ramakrishna, A., and Ramji, K., "CFD Analysis of a Propeller Flow and Cavitation," *International Journal of Computer Applications*, vol. 55, 2012, pp. 26–33.
29. Rossow, V. J., "Technical Notes: Thrust Changes Induced by Ground and Ceiling Planes on a Rotor in Hover," *Journal of the American Helicopter Society*, vol. 30, Jan. 1985, pp. 53–55.
30. Rumsey, C. L., and Ying, S. X., "Prediction of high lift: review of present CFD capability," *Progress in Aerospace Sciences*, vol. 38, 2002, pp. 145–180.
31. Sipila, T., Siikonen, T., and Saisto, I., "FINFLO RANS-Predictions for Propeller Performance," *Second International Symposium on Marine Propulsors*, June 2011.
32. Turner, R. S., "Design and Optimisation of a Propeller for a Micro Air Vehicle Using Computational Fluid Dynamics," University of New South Wales at the Australian Defence Force Academy, 2010.
33. UIUC Propeller Data Site Available: <https://m-selig.ae.illinois.edu/props/propDB.html>.

34. Walters, D. K., & Cokljat, D., "A Three-Equation Eddy-Viscosity Model for Reynolds-Averaged Navier–Stokes Simulations of Transitional Flow," *Journal of Fluids Engineering*, 130(12), 121401, 2008. doi:10.1115/1.2979230.
35. Wheeler, A. J., and Ganji, A. R., *Introduction to Engineering Experimentation*, Boston: Prentice Hall, 2010.
36. Zhang, C., Xie, S., and Qin, T., "Aerodynamic Analysis of Small Propeller in Wind Field Using CFD," *Proceedings of the 2015 4th International Conference on Sustainable Energy and Environmental Engineering*, 2016.